

Observational correlation between magnetic field, angular momentum, and fragmentation in the envelopes of Class 0 protostars?

Maud Galametz¹, Anaëlle Maury^{1,2}, Josep M. Girart^{3,4}, Ramprasad Rao², Qizhou Zhang², Mathilde Gaudel⁵, Valeska Valdivia¹, Patrick Hennebelle¹, Victoria Cabedo-Soto¹, Eric Keto², Shih-Ping Lai⁶

¹ Astrophysics department, CEA/DRF/IRFU/Dap, Université Paris Saclay, UMR AIM, F-91191 Gif-sur-Yvette, France, e-mail: maud.galametz@cea.fr

² Center for Astrophysics | Harvard & Smithsonian, 60 Garden street, Cambridge, MA 02138, USA

³ Institut de Ciències de l'Espai (ICE, CSIC), Can Magrans, S/N, E-08193 Cerdanyola del Vallès, Catalonia, Spain

⁴ Institut d'Estudis Espacials de Catalunya (IEEC), E-08034 Barcelona, Catalonia, Spain

⁵ LERMA, Observatoire de Paris, 61 av. de l'Observatoire F-75014 Paris, France

⁶ Institute of Astronomy and Department of Physics, National Tsing Hua University, Hsinchu 30013, Taiwan

Preprint online version: October 11, 2021

ABSTRACT

Aims. Our main goal in this analysis is to assess the potential role of magnetic fields in regulating the envelope rotation, the formation of disks, and the fragmentation of Class 0 protostars in multiple systems.

Methods. We used the Submillimeter Array to carry out observations of the dust polarized emission at 0.87 mm in the envelopes of a large sample of 20 Class 0 protostars. We estimated the mean magnetic field orientation over the central 1000 au envelope scales to characterize the orientation of the main component of the organized magnetic field at the envelope scales in these embedded protostars. This direction was compared to that of the protostellar outflow in order to study the relation of their misalignment and the kinematics of the circumstellar gas. The latter is traced through the velocity gradient that is observed in the molecular line emission (mainly N_2H^+) of the gas at intermediate envelope scales.

Results. We discover that the misalignment of the magnetic field orientation is strongly related to the outflow and the amount of angular momentum observed at similar scales in the protostellar envelope. This reveals a potential link between the kinetic and the magnetic energy at envelope scales. The relation could be driven by favored B-misalignments in more dynamical envelopes or by a dependence of the envelope dynamics on the initial large-scale B configuration. By comparing the trend with the presence of fragmentation, we observe that single sources are mostly associated with conditions of low angular momentum in the inner envelope and good alignment of the magnetic field with protostellar outflows at intermediate scales. Our results suggest that the properties of the magnetic field in protostellar envelopes are tightly related to the rotating infalling gas that is directly involved in the formation of stars and disks: we find that it may not only affect the fragmentation of protostellar cores into multiple stellar systems, but also sets the conditions that establish the pristine properties of planet-forming disks.

Key words. Stars: formation, protostars, low-mass, circumstellar matter – ISM: magnetic fields, kinematics and dynamics – Submillimeter: ISM – Instrumentation: interferometers, polarimeters – Methods: observational

1. Introduction

A majority of stars in our Galaxy are found in multiple stellar systems, and a significant fraction of solar-type stars will host planetary systems (Duchêne & Kraus 2013; Hsu et al. 2019). Most of the final stellar mass is collected during a short but vigorous accretion phase. During this so-called protostellar phase, the star forms at the center of an infalling rotating core, concomitantly with a surrounding disk of gas in circular orbits around the star: while the star will inherit the majority of the accreted mass, most of the angular momentum contained in the protostellar envelope is expected to be expelled or stored in the protostellar disk. This evolution will eventually lead to protoplanetary systems (Zhao et al. 2020). Class 0 objects are the youngest accreting protostars and are surrounded by a dense envelope that is accreted onto the central protostellar embryo during a short ($t < 5 \times 10^4$ yr) accretion phase (André et al. 2000; Evans et al. 2009). Characterizing the dynamics of the gas and the physical processes of these youngest protostars is crucial for understanding

the efficiency of the star formation process, the global properties of stars in our Galaxy, and the setting of the conditions that allow disks and planets to form around them.

Magnetic fields (hereafter B) are ubiquitous in the Universe (Vallée 2004) and have been observed to permeate the interstellar material deep down into star-forming cores and protostellar environments (Girart et al. 2006; Hull & Zhang 2019). From a theoretical point of view, the presence of B in star-forming cores has been shown to significantly alter the dynamics of the gas participating in the building of stars during the accretion phase, and it affects the resulting properties of these stars and associated circumstellar disks (Terebey et al. 1984; Wurster & Li 2018; Hennebelle & Inutsuka 2019). The mechanism for evacuating angular momentum from the infalling gas through magnetic torques applied by Alfvén waves is called magnetic braking. The initial global collapse, driven by gravity, drags the field lines, which leads to an hourglass morphology of the field lines and amplifies the magnetic intensity. The magnetic braking

seems to be particularly enhanced by the pinching of field lines, which lengthens the magnetic lever arms and efficiently transports the angular momentum from the inner envelope toward the outer one (Galli et al. 2006). As less angular momentum is transported toward the forming star, only small protoplanetary disks form while the star grows (Allen et al. 2003; Hennebelle & Fromang 2008; Masson et al. 2016; Hirano & Machida 2019).

The importance of the misalignment between magnetic field and rotation axis has been stressed by several authors (Ciardi & Hennebelle 2010; Joos et al. 2012; Gray et al. 2018). They found that in ideal magnetohydrodynamic (MHD) calculations, only small disks form or even no disk forms in the aligned configurations when the field is strong enough; and it is comparatively far easier to form a disk in the misaligned case. Numerical simulations taking into account non-ideal MHD effects (such as ambipolar diffusion or Hall effect) were able to overcome the magnetic braking catastrophe, leading to the formation of disks similar to those observed (Hennebelle et al. 2016; Zhao et al. 2018; Wurster & Bate 2019). Studies by Hennebelle et al. (2020) or Wurster & Lewis (2020) appear to also predict that the misalignment of the magnetic field with the envelope rotation axis directly affects the protostellar disk formation, for instance, leading to the formation of larger planet-forming disks in the misaligned cases that were investigated compared to the smaller disks that are observed in aligned cases. This is particularly clear when the field intensity is such that the mass-to-flux ratio is on the order of 10. Another key prediction of magnetized models is that a strong, organized B partly alters the ability of the envelope to fragment. This suggests that B is one of the regulating agents that drive the birth of the multiple stellar systems we commonly observe in the Galaxy (Hennebelle & Teyssier 2008).

The effect of the various characteristics of the B field (orientation with the collapse direction and strength), however, is poorly quantified observationally speaking. Only a few studies have attempted to test the predicted relation that links the B-field orientation in protostellar cores to the magnitude of the angular momentum of the gas responsible for disk properties and the formation of multiple stellar systems (see, e.g., the works of Chapman et al. 2013; Hull et al. 2013; Zhang et al. 2014). Because it is difficult to trace B in these small embedded astrophysical structures, it has so far been difficult to reach the statistical significance that would allow us to draw firm conclusions about the role of magnetic braking in the formation of stars and disks (Yen et al. 2015a; Maury et al. 2018). In order to statistically investigate the B-field orientation, we carried out a SubMillimeter Array (SMA) survey of 20 low-mass Class 0 protostars, using 0.87 mm polarized dust emission. Because asymmetric dust particles of the interstellar medium align themselves with their minor axis parallel to the B-field lines (Andersson et al. 2015), the observed polarized angle provides us with a robust proxy of the direction perpendicular to the magnetic field orientation. Class 0 objects were ideally suited for this analysis because most of the mass that collapses onto the central embryo still resides in the envelope, allowing us to trace the B orientation at envelope (1000-2000 au) scales. Galametz et al. (2018) presented results for a first subsample of 12 sources, focusing on the properties of polarization fractions and general alignment between B and the outflow at envelope scales. We reported the detection of linearly polarized dust emission in all the objects of the sample. By comparing the B orientation with that of the outflow axis, which is commonly used as a proxy for the rotational axes of these systems, we noted that at the scales traced in our analysis, the B-field lines were preferentially misaligned in sources for which large equatorial velocity gradients were re-

ported in the literature. A potential link between the envelope dynamics and the B orientation might be an additional signature that B has a strong effect on the collapse and fragmentation, as has also been suggested by the analysis of massive cores by Zhang et al. (2014).

We complement the Galametz et al. (2018) observations with eight additional Class 0 envelopes observed with the SMA at 0.87mm at comparable scales. The full SMA B measurements are combined with gas kinematics information obtained homogeneously from N_2H^+ observations of velocity gradients in the envelopes, either from the Continuum And Lines in Young ProtoStellar Objects survey (CALYPSO; Maury et al. 2019; Gaudel et al. 2020, seven sources) or from observations published in the literature that we reprocessed when required (12 sources, see Table 4). Our goal is to observationally test the theoretical predictions of the conditions required for magnetic braking affecting the collapse and assess the potential role of B in regulating the matter infall and envelope rotation, the formation of disks, and the fragmentation into multiple systems.

2. Observations

2.1. Sample description

Galametz et al. (2018) presented 12 low-mass Class 0 protostars observed in polarization at 345 GHz with the SMA. We complement this first subsample with 8 additional low-mass protostars. The 20 sources cover a wide range of protostellar properties: isolated, binary, triple, or quadruple systems form in cores whose masses range from 0.2 to $12M_{\odot}$. Details of the full sample are provided in Table 1.

2.2. SMA dust polarization observations

The observations (taken in both compact and sub-compact configurations), data reduction and polarization maps of the first 12 low-mass Class 0 protostars observed are presented in Galametz et al. (2018). The observations of the 8 additional low-mass protostars were obtained with the SMA settled in compact configuration in the 345 GHz band (Project 2018B-S015, PI: A. Maury). The antennas used for each observation date are listed in Table 2. The polarimeter on the SMA makes use of a quarter-wave plate (QWP) in order to convert the linear polarization into circular polarization. The antennas are switched between polarizations (QWP are rotated at various angles) in a coordinated temporal sequence to sample the various combinations of circular polarizations on each baseline. A variety of observational modes (single- and dual-receiver polarization modes) were used for the observations of Galametz et al. (2018). The dual-receiver full polarization mode, fully commissioned, was then the only mode we used to observe the additional 8 targets. The new observations were also taken using the SMA Wideband Astronomical ROACH2 Machine (SWARM) rather than the Application-Specific Integrated Circuit (ASIC) correlator: the added bandwidth has helped increase the SMA sensitivity. A detailed description of the SMA polarimeter system is provided by Marrone (2006) and Marrone & Rao (2008). Frequent observations of various calibrators were taken between the target observations to ensure the future gain and polarization calibration. Flux calibrators (Callisto and Neptune) were also observed, but were not used when we performed the flux calibration of the observations (see § 2.3).

Table 1. Characteristics of the full sample.

| Name | α (J2000) | δ (J2000) | Cloud | Distance (pc) | M_{env} | References |
|---------------------------------|------------------|------------------|-------------------|---------------|------------------|------------|
| Per B1-bS ^a | 03:33:21.35 | +31:07:26.4 | Perseus / Barnard | 230 | 3.0 | [2, 12] |
| Per B1-c ^a | 03:33:17.88 | +31:09:32.0 | Perseus / Barnard | 230 | 2.1 | [2, 11] |
| B335 | 19:37:00.90 | +07:34:09.6 | isolated | 100 | 1.3 ^b | [3, 15] |
| BHR7-MMS ^a | 08:14:23.33 | -34:31:03.7 | Gum / Vela | 400 | 1.0 | [5, 13] |
| CB230 | 21:17:40.00 | +68:17:32.0 | Cepheus | 352 | 3.4 | [4, 14] |
| HH25-MMS ^a | 05:46:07.40 | -00:13:43.4 | Orion / L1630 | 400 | 0.5 | [6, 16] |
| HH211-mm ^a | 03:43:56.52 | +32:00:52.8 | Perseus / IC348 | 320 | 1.5 | [1, 16] |
| HH212 [*] | 05:43:51.40 | -01:02:53.0 | Orion / L1630 | 400 | 0.2 | [6, 17] |
| HH797 | 03:43:57.10 | +32:03:05.6 | Perseus / IC348 | 320 | 1.1 | [1, 19] |
| IRAS03282 | 03:31:20.40 | +30:45:24.7 | Perseus | 293 | 2.2 | [1, 18] |
| IRAS16293-A | 16:32:22.9 | -24:28:36.0 | Ophiuchus | 150 | 2.3 | [8, 16] |
| L1157 | 20:39:06.3 | +68:02:15.8 | Cepheus | 352 | 3.0 | [4, 10] |
| L1448C | 03:25:38.9 | +30:44:05.4 | Perseus | 293 | 2.0 | [1, 10] |
| L1448N-B | 03:25:36.3 | +30:45:14.9 | Perseus | 293 | 4.8 | [1, 10] |
| L1448-2A | 03:25:22.4 | +30:45:13.0 | Perseus | 293 | 1.9 | [1, 10] |
| L483-mm ^a | 18:17:29.94 | -04:39:39.3 | Serpens Cirrus | 250 | 1.8 | [7, 18] |
| NGC 1333 IRAS4A | 03:29:10.5 | +31:13:31.0 | Perseus | 293 | 12.3 | [1, 10] |
| NGC 1333 IRAS4B | 03:29:12.0 | +31:13:08.0 | Perseus | 293 | 4.7 | [1, 10] |
| Serpens South MM18 ^a | 18:30:04.12 | -02:03:02.55 | Serpens South | 350 | 5 | [9, 10] |
| SVS13-B | 03:29:03.1 | +31:15:52.0 | Perseus | 293 | 2.8 | [1, 10] |

^a Sources whose SMA polarization observations are described in this paper. The polarization results for the remaining sources are described in Galametz et al. (2018), Girart et al. (2014), and Rao et al. (2009).

^b The total globule mass is probably a factor of 3-5 higher (Stutz et al. 2008).

References for the distances and M_{env} - [1] Ortiz-León et al. (2018a), [2] Černis & Straizys (2003), [3] Olofsson & Olofsson (2009), [4] Zucker et al. (2019), [5] Woermann et al. (2001), [6] Anthony-Twarog (1982) [7] Herczeg et al. (2019) [8] Ortiz-León et al. (2018b), [9] Ongoing work re-analyzing the Gaia data toward Serpens South suggests a high extinction layer up to distances of 350 pc (Palmeirim, André et al. in prep). We use this reevaluated distance. [10] Maret et al. (2020), [11] Matthews et al. (2006), [12] Andersen et al. (2019), [13] Tobin et al. (2018), [14] Massi et al. (2008), [15] Launhardt et al. (2013), [16] André et al. (2000), [17] Wiseman et al. (2001), [18] Tobin et al. (2011), [19] Sadavoy et al. (2014).

Table 2. Details of the observations ^a

| Date | Gain calibrator | Polarization calibrator | Antenna used | Flux cal. scaling factor ^b |
|-------------|----------------------------------------|-------------------------|------------------------|---------------------------------------|
| Nov 27 2018 | 1925+211, 0336+323, 3C 84, 0747-331 | 3C 454.3, 3C 84 | 1, 2, 3, 4, 5, 6, 7, 8 | 1.7 |
| Nov 28 2018 | 0336+323, 3C 84, 0747-331 | 3C 454.3, 3C 84 | 2, 3, 4, 5, 6, 8 | 1.5 |
| Nov 29 2018 | 0336+323, 0747-331, 0607-085, 0532+075 | 3C 454.3 3C 84 | 3, 4, 5, 6, 7, 8 | 1.4 |
| Dec 05 2018 | 0336+323, 0607-085, 0532+075, 0747-331 | 3C 84, 3C 279, 3C 454.3 | 1, 3, 4, 5, 6, 8 | 1.2 |
| Dec 06 2018 | 0336+323, 0607-085, 0532+075 | 3C 454.3, 3C 279 | 1, 3, 4, 5, 6, 8 | 1.3 |
| Dec 07 2018 | 0532+075, 0607-085 | 3C 279 | 1, 2, 3, 4, 5, 6, 8 | 1.4 |
| Apr 15 2019 | 1733-130, 1751+096, 1924-292, mwc349a | 3C 279, 3C 273 | 1, 2, 3, 5, 7, 8 | 0.9 |
| Apr 16 2019 | 1733-130, 1751+096 | 3C 279, 3C 273 | 1, 2, 3, 5, 7, 8 | 0.9 |

^a Details of the observations for the first half of the sample are presented in Galametz et al. (2018).

^b Scaling factors derived by comparing the quasars observed with the SMA with their fluxes at similar dates in the ALMA calibration source catalog.

2.3. Data reduction, self-calibration, and flux calibration

We performed the data reduction on the raw visibilities using the IDL-based software MIR (for Millimeter Interferometer Reduction). The calibration includes an initial flagging of high system temperatures T_{sys} and other incorrect visibilities, a band-pass calibration, a correction of the cross-receiver delays, and a gain and flux calibration. The various calibrators observed for each of these steps and the list of antennas used for the observations are summarized in Table 2. Data were then exported to

MIRIAD (Sault et al. 1995)¹ for additional processing (i.e., additional flagging) and in particular to perform the instrumental polarization calibration. Quasars were observed to calculate the leakage terms. The continuum data of the targets were used to perform an iterative self-calibration of the Stokes I visibilities. The process was repeated with deeper cleans and shorter intervals until it converged (no rms improvement). We finally used the Atacama Large Millimeter/submillimeter Array (ALMA)

¹ <https://www.cfa.harvard.edu/sma/miriad/>

Table 3. Characteristics of the SMA maps ^a

| Name | Synthesized beam | rms | | | in the 0.87mm reconstructed map | | |
|---------------|-------------------|----------------|-----|-----|---------------------------------|-----------------------------------|-------------------------------------|
| | | I ^b | Q | U | Peak intensity (Jy/beam) | Peak P _i (mJy/beam) | P _{frac} ^c % |
| Per B1-bS | 2".1×1".2 (-54°) | 4.0 | 1.2 | 1.3 | 0.46 | 5.1 | 5.3 |
| Per B1c | 1".8×1".3 (-58°) | 4.0 | 2.3 | 2.4 | 0.44 | 8.2 | 7.5 |
| BHR7-MMS | 2".7×1".3 (-29°) | 2.5 | 1.1 | 1.1 | 0.53 | 4.5 | 0.8 |
| HH25-MMS | 1".7×1".5 (-67°) | 3.4 | 1.9 | 1.9 | 0.25 | 6.2 | - |
| HH211-mm | 1".5×1".4 (71°) | 1.2 | 0.7 | 0.7 | 0.17 | 2.3 | 3.3 |
| HH212 | 1".7×1".3 (-81°) | 0.6 | 0.2 | 0.2 | 0.19 | 2.1 | 3.0 |
| L483-mm | 1".9 × 1".5 (30°) | 1.6 | 1.3 | 1.2 | 0.10 | 2.7 | 13.6 |
| Serpens SMM18 | 1".9×1".5 (34°) | 11.3 | 1.9 | 2.0 | 0.86 | 19.4 | 3.8 |

^a Details of the SMA maps for the first half of the sample are presented in Galametz et al. (2018).

^b after self-calibration.

^c Mean polarization fraction defined as the unweighted ratio between the mean polarization over total flux.

calibration source catalog² to gather the fluxes of quasars we also observed with the SMA (3C 84, 3C 454.3, 3C 273, and 3C 279) at similar dates as those of our observations. These fluxes were compared to the SMA amplitudes in order to derive the multiplying factors that were to be applied to the target visibility amplitude in order to flux-calibrate the dataset. These scaling factors are reported for each date in Table 2. The visibilities covered by the observations range from 15 to 85 kλ.

2.4. Deriving the continuum and polarization maps

The Stokes parameters are defined as

$$\vec{S} = \begin{bmatrix} I \\ Q \\ U \\ V \end{bmatrix}, \quad (1)$$

with Q and U the linear polarization and V the circular polarization. We used a robust weighting of 0.5 to transform the visibility data into a dirty map (using the MIRIAD *invert* task). We produced cleaned images of the various Stokes parameters (using the MIRIAD *clean* task). Finally, maps of the polarized intensity (debiased) P_i, polarization fraction p_{frac}, and polarization angle P.A. were produced (using the MIRIAD *impol* task) as follows:

$$P_i = \sqrt{Q^2 + U^2 - \sigma_{Q,U}^2}, \quad (2)$$

$$p_{frac} = P_i / I, \quad (3)$$

$$P.A. = 0.5 \times \arctan(U/Q), \quad (4)$$

with $\sigma_{Q,U}$ the average rms of the Q and U maps. We applied a 5σ cutoff on Stokes I and a 3σ cutoff on Stokes Q and U in order to only discuss locations where polarized emission is robustly detected. The synthesized beams and rms of the various cleaned maps are provided in Table 3. Maps are produced with a pixel size of 0.6". In the appendix (see Table B.1), we show that this choice does not affect the mean B-field orientation we derived.

The Stokes I dust continuum emission maps are shown in Fig. 1. A description of the morphology of this continuum emission as well as details of the source multiplicity are provided in Appendix A. The polarized intensity and polarization fraction maps are shown in Fig. D.1. To our knowledge, we present the

first detections of polarized dust emission at envelope scales toward BHR7 and HH25.

3. Analysis

3.1. Mean magnetic field orientation

The polarization angles were rotated by 90° to obtain the magnetic field direction. The B vectors obtained for the 20 sources are overlaid on the Stokes I maps in Fig. 1. We note that the strength of SMA observations is twofold. First, their interferometric nature allows us to filter out the large-scale B field permeating the surrounding host cloud, and we focus on the fields in the inner protostellar envelopes. Second, the modest spatial resolution of our observations allows us to cancel out the more complex topology of the field at small (< 500 au) scales because of the intense gravitational pull of the infalling material and the launching of protostellar outflows (Kwon et al. 2019). Our observations are also expected to be less prone than high-angular resolution observations to selectively tracing the B field in locations where the dust grain alignment efficiency may be highly inhomogeneous, for instance, along irradiated cavity walls that are located very close to the central protostellar objects (see, e.g., Le Gouellec et al. 2019). Because most Class 0 disks only contribute at scales much smaller than the scales probed by our beam (fewer than 25% of the Class 0 disks extend beyond 60 au; see Maury et al. 2019), dust polarization due to self-scattering is unlikely to contribute to the polarization observed at envelope scales with the SMA.

To trace the main direction of B at envelope scales, we extracted the mean B-field orientation within the central 1000 au region of each source. To perform the calculation, we used the polarization angle and polarization angle error maps produced with our data-reduction procedure within the *idl/wmean* function. The weighted mean is calculated as

$$\mu = \frac{\sum x_i / \sigma_i^2}{\sum 1 / \sigma_i^2}, \quad (5)$$

with μ the mean position angle of the B field, x_i the individual position angles detected within the central 1000 au region, and σ_i their associated errors. We report the magnetic field position angles in Table 4 and overlay them (with red segments) on the Stokes I maps for the full sample in Fig. 2. The errors provided in Table 4 are the external uncertainties *eu* based on the spread

² <https://almascience.eso.org/sc/>

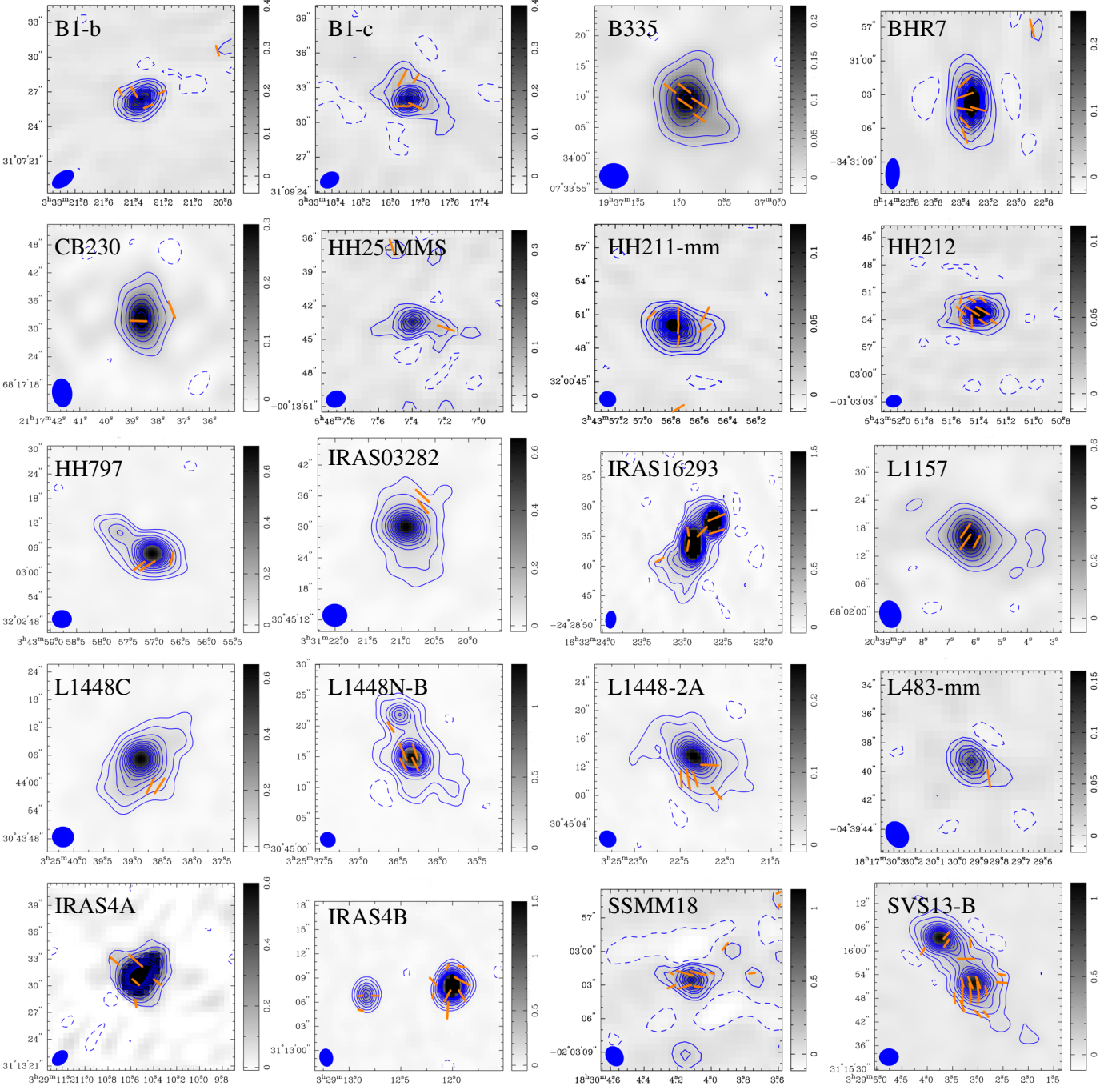


Fig. 1. B-field vectors (derived from the polarization vectors assuming a 90° rotation) overlaid as orange segments on the SMA $850\ \mu\text{m}$ Stokes I continuum maps. Color scales are in Jy/beam . Contours at $-3, 5, 10, 20, 30, 40, 50, 60, 70, 80, 90,$ and $100\ \sigma$ appear in blue. The filled ellipses in the lower left corner indicate the synthesized beam of the SMA maps.

of the values obtained multiplying the internal uncertainty iu by the square-root of the reduced chi-squared, with

$$iu = \frac{1}{\sqrt{\sum 1/\sigma_i^2}} \quad (6)$$

and

$$eu = iu \sqrt{\frac{\chi^2}{N-1}} \quad \text{where} \quad \chi^2 = \sum \frac{(x_i - \mu)^2}{\sigma_i^2}. \quad (7)$$

This method is appropriate for calculating a mean B-field angle recovered at $1000\ \text{au}$ scales in protostellar envelopes, from individual detections presenting a large dynamic range in signal-to-noise ratios, as are some of the polarization detections in the SMA map of each individual source, but also to propagate the individual errors and angle dispersions into an error on the mean value. While most protostars show small dispersions of their individual detections around the mean B field (18 sources out of 20 have dispersions $< 20^\circ$), we note that two protostars (IRAS16293A and Per-B1c) present large angle dispersions

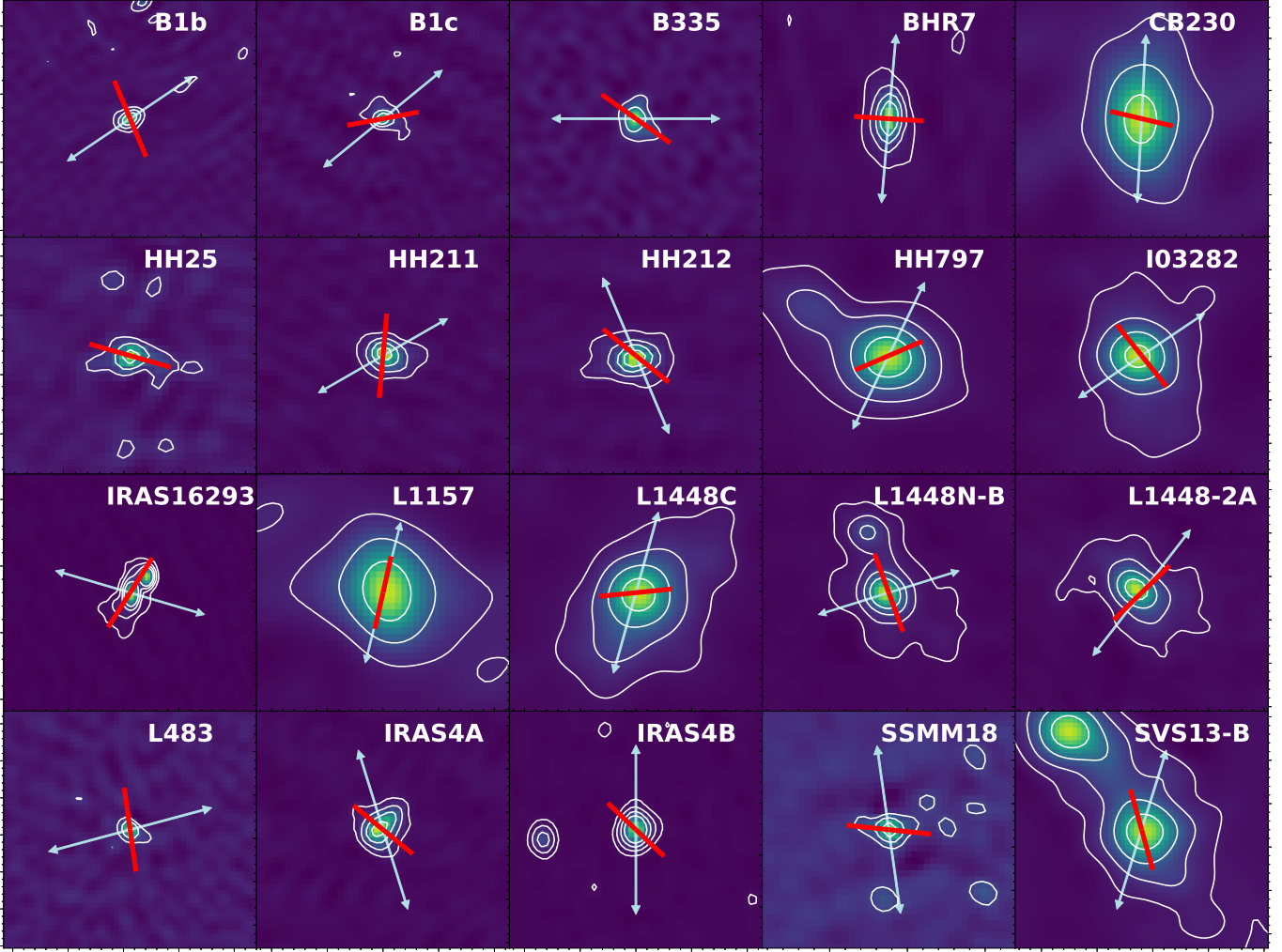


Fig. 2. Mean magnetic field orientation in the 20 Class 0 protostellar envelopes (red segments) overlaid on the dust emission maps (contour and color maps). Contours are indicated for detections at 5, 20, 50, and 100 σ . The common physical scale of each map is 8000×8000 au. We indicate the outflow axis for each source with cyan arrows. For L1448C, we report the central 2- σ detection (see Galametz et al. 2018, and §3.1.).

around their mean position angle.

To quantify the effect of the pixel size that we used during the map-making procedure on the mean B-field orientation, we rederived the polarization maps for pixels equal to 0.6'' (our fiducial pixel scale), 0.7'' , 0.8'' , 0.9'' , and 1.0'' and reestimated the mean magnetic field position angles (see Table B.1). We observe that the pixel size affects the position angles we derived only very little; the uncertainties on the orientation are mostly dominated by the dispersion of the position angles within the 1000 au central region. We note that for HH211, the interval of values obtained by changing the pixel size ranges from 162° to 175°: the error in position angle may be closer to 10° than the 5° we report in Table 4 for this source.

Additionally, because other methods have been developed for calculating mean polarization angles, we propose in Appendix C a simple comparison between the mean angles obtained from our method and three other averaging methods that are used to analyze single-dish observations of dust po-

larized emission. The three additional methods rely on (i) a simple averaging (no weighting), (ii) an averaging of the Stokes values before computing an angle (e.g., used in the single-dish maps of clouds by Li et al. 2006), or (iii) summing individual Stokes fluxes to remove the variations around a mean value (considering that Stokes Q and U are positive and negative, their sum cancels most variations and should converge toward the most widespread value in the map). This second test shows that the position angle of the mean B field computed with the different methods presents only small variations in the mean position angle, with a dispersion smaller than the error bars from our method reported in Table 4. This indicates that our measurement are robust envelope-scale values. One exception is HH212, for which the interval of values obtained using the various methods ranges from 51 to 59°. As for HH211, the error on position angle may be closer to 10° than the 4° error reported in Table 4 for this source.

The magnetic field orientation of 12 sources of the sample is discussed in Galametz et al. (2018). We add here additional

notes concerning the choices we made in the current analysis. For IRAS4B, the B field is complex, with an average B-field direction in the eastern part of $149\pm 45^\circ$ and an average direction in the western part of $51\pm 19^\circ$. Both sides give a misalignment with the outflow of $30\text{--}50^\circ$. In this analysis, we used a misalignment of 40° for this source. The B-field orientation used for IRAS03292 is the average value detected in the off-centered region where B is detected by the SMA (see Galametz et al. 2018). In the case of L1448C, the only robust detections ($>3\text{-}\sigma$) are vectors located outside the central 1000 au region, as shown in our Fig. 1. For this analysis, we thus decided to report the $2\text{-}\sigma$ detection of the polarized dust emission in the central region from Galametz et al. (2018): its position angle is in agreement with the 1.3 mm B-field detections reported by Hull et al. (2014) (e.g. a P.A. of 95°). We stress that the B-field topology in the outer envelope layers may be complex (Cox et al. 2018) and differ from the main B-field reported here. For L1448-2A, the hourglass shape is resolved with the SMA: we therefore used the central vector detected in the TADPOL survey (Hull et al. 2014). Finally, for IRAS16293-A, we estimated the mean magnetic field orientation in a smaller ($3''$ in radius) aperture to avoid contamination by the companion source IRAS16293-B. The average value ($173\pm 40^\circ$) is consistent with the NS orientation also found in Rao et al. (2009), and the uncertainty is large.

We provide details of the magnetic field orientation of the additional eight sources in Appendix A. Most of the additional sources present misaligned configurations between the B and outflow position angles. For B1-bS, we note that we decided to use the average north-east value for our analysis because apparently it better traces the magnetic field at envelope scales connected with the field traced on larger scales. For L483, the eastern line segment shows a discrepancy with the global orientation of the western line segments: we did not include it in our analysis (see the discussion in Appendix A, which shows that this choice does not affect the correlation we find, however).

Finally, Table 4 also provides the outflow position angles retrieved from the literature (see references in the table). The outflow position angle uncertainties can vary from one source to another and depend on the outflow inclination and potential overlap of the red- and blueshifted components. We assumed a conservative 10° error on the outflow position angle for all sources.

3.2. Kinematic properties of the protostellar envelopes

The CALYPSO sources. For sources that are part of the CALYPSO sample (i.e., L1157, L1448C, L1448N-B, L1448-2A, IRAS4A, IRAS4B, and SVS13-B), Gaudel et al. (2020) recently presented observations of the dense gas kinematics using C^{18}O and N_2H^+ measurements. They derived specific angular momentum estimates throughout their collapsing protostellar envelopes from 50 au to 10000 au scales. In their analysis, velocity maps are produced from a combined Plateau de Bure (PdBI) + 30-m N_2H^+ dataset. A hyperfine structure line profile was used to determine the velocity of the molecular line emission in order to produce a velocity map. Then velocity gradients were fit in a $40'' \times 40''$ region around the sources and determined by the least-squares minimization, with $v_{grad} = v_0 + a\Delta\alpha + b\Delta\beta$, with $\Delta\alpha$ and $\Delta\beta$ the offsets with respect to the central source (Goodman et al. 1993). Serp SMM18 is also part of the CALYPSO sample but is not included in the sample studied in Gaudel et al. (2020). For this source, we determined the velocity gradient strength and position angle using the same 2D fit-

ting technique. The velocity map is shown in the appendix in Fig. E.1.

CB230, HH211-mm, IRAS03282, and L483. For these sources, 2D velocity gradients and position angles on similar scales have been estimated in Tobin et al. (2011) using the N_2H^+ line and fitting a plane to the entire velocity field (with $R > 10''$ for L483 and R of about $20\text{--}25''$ for the other sources). We use their velocity gradients and position angles in the following analysis (see their Table 10). L1157 is also part of their sample, with a greater velocity gradient strength (from 3.5 to $10.5 \text{ km s}^{-1} \text{ pc}^{-1}$) than was derived in Gaudel et al. (2020) ($0.8 \text{ km s}^{-1} \text{ pc}^{-1}$) and different position angles depending on the use of PdBI, Combined Array for Research in Millimeter-wave Astronomy (CARMA), or Very Large Array (VLA) data. We kept the values from Gaudel et al. (2020) in this paper, but recall that the N_2H^+ velocity field is extremely complex for this source: the velocity gradient direction is close to the outflow axis, but the symmetry is perturbed by a redshifted line emission southeast of the protostar, with potential contribution of the outflow cavity walls to the N_2H^+ emission for this source (Tobin et al. 2011; Gaudel et al. 2020).

Per B1-bS. We calculated the 2D velocity gradients from the N_2D^+ datacube obtained from N. Hirano and presented in Huang & Hirano (2013). Compared to its companion source B1-bN, the B1-bS line profiles are dominated by the $V_{LSR} = 6.3 \text{ km s}^{-1}$ component. We fit this hyperfine structure with the *hfs_cube* procedure (Estalella 2017), fitting the line when detected at a 5σ level. The procedure returns a velocity map from which we determined the gradient on a $20'' \times 20''$ region around the source to avoid contamination by the companion. The map of the gas velocities in the envelope of B1-bS that we used to extract the main velocity gradient in this source is shown in Fig. E.1. Because a smaller region was fit, the magnitude of the velocity gradient might only provide an upper limit for this source: velocity gradients tend to increase when probed at smaller physical radii, as shown, for instance, by Gaudel et al. (2020) (their Table 2).

Per B1-c. We calculated the 2D velocity gradients from the N_2H^+ velocity map obtained from B. Matthews and presented in Matthews et al. (2006). As explained in their analysis, the spectral resolution was not sufficient to separate the hyperfine splitting components, therefore the moment map was taken over an isolated line component of N_2H^+ . The velocity map of this source is presented in Fig. E.1. We fit the velocity gradient in a $20'' \times 20''$ region around the source to encompass the full N_2H^+ emission presented in Matthews et al. (2006) (their Fig. 8). As for Per B1-bS, the magnitude of the velocity gradient might provide an upper limit for this source because a smaller region was fit.

BHR7-MMS. We calculated the 2D velocity gradients from both the H_2CO and N_2D^+ datacubes obtained from J. Tobin and presented in Tobin et al. (2018). We used Gaussian line profiles to model the H_2CO emission and the *hfs_cube* procedure (Estalella 2017), fitting the hyperfine structure of the N_2D^+ line when detected at a 5σ level. For H_2CO , as there is no robust detection beyond a radius of $7''$ (equivalent to 3000 au for BHR7), we estimated the velocity gradient in a $14'' \times 14''$ region around the source and obtained a gradient of $40 \text{ km s}^{-1} \text{ pc}^{-1}$. We note, however, that in the cold envelope, there might not be enough CO in the gas phase to form H_2CO : a significant part of the H_2CO emission could thus come from warmer gas belonging to the outflow, as suggested by the position angle (-19° , thus aligned with the outflow) of the velocity gradient we derive. In

Table 4. Position angles of the outflow and magnetic field and velocity gradient characteristics

| Name | Outflow | | B_{mean} | Line used | Velocity gradients | | |
|-----------------|--------------------------|------|--------------------|------------------------|--------------------------------------------------|-------------|--------------|
| | P.A. ^a (°) | Ref. | P.A. (°) | | Gradient ($\text{km s}^{-1}\text{pc}^{-1}$) | P.A. (°) | Ref. |
| Per B1-bS | 120 | [1] | 26±7 | N_2D^+ | 23±3 | -8±8 | [26] & T. w. |
| Per B1c | 125 | [2] | 99±39 | N_2H^+ | 7.5 | 50 | [2] & T. w. |
| B335 | 90 | [3] | 55±3 | N_2H^+ | ~1.0 | - | [24] |
| BHR7-MMS | 174 | [4] | 87±19 | N_2D^+ | 14±1.0 | -36±6 | [4] & T. w. |
| CB230 | 172 | [5] | 85±4 | N_2H^+ | 3±0.1 | 98±1.3 | [21] |
| HH25-MMS | - | [6] | 74±17 | - | - | - | - |
| HH211-mm | 116 | [7] | 174±5 | N_2H^+ | 7±0.03 | 26±0.3 | [21,23] |
| HH212 | 23 | [8] | 51±4 | NH_3 | 4.5 | 113 | [22] |
| HH797 | 150 | [9] | 110±7 | - | - | - | - |
| IRAS03282 | 120 | [10] | 43±6 | N_2H^+ | 9±0.01 | 114±0.01 | [21] |
| IRAS16293-A | 75 & 145 | [11] | 173±40 | CN | 25 | - | [25] |
| L1157 | 146 | [12] | 149±4 | N_2H^+ | 0.8±0.4 | 113±65 | [20] |
| L1448C | 162 | [13] | 95±4 | N_2H^+ | 13±1 | -179±1.0 | [20] |
| L1448N-B | 105 | [14] | 23±4 | N_2H^+ | 13±1 | 100±1 | [20] |
| L1448-2A | 134 | [5] | 139±9 ^b | N_2H^+ | 2±1 | -177±21 | [20] |
| L483 | 105 | [15] | 8±11 | N_2H^+ | 9±0.03 | 45±0.2 | [21] |
| NGC 1333 IRAS4A | 20 | [16] | 55±13 | N_2H^+ | 7±1 | 37±2 | [20] |
| NGC 1333 IRAS4B | 0 | [17] | 51±19 | N_2H^+ | 3±1 | -71±14 | [20] |
| Serp SMM18 | 8 | [18] | 84±16 | N_2H^+ | 12±0.01 | 69±0.04 | T. w. |
| SVS13-B | 160 | [19] | 18±5 | N_2H^+ | 5±1 | 16±4 | [20] |

^a Position angles in the table are provided east of north.

^b Taken from Hull et al. (2013).

References - T. w. refers to this work, [1] Gerin et al. (2015), [2] Matthews et al. (2008), [3] Hirano et al. (1988), [4] Tobin et al. (2018), [5] Hull et al. (2013), [6] Dunham et al. (2014), [7] Gueth & Guilloteau (1999), [8] Lee et al. (2017), [9] Tafalla et al. (2006), [10] Hatchell et al. (2007), [11] Rao et al. (2009), [12] Bachiller et al. (2001), [13] Dutrey et al. (1997), [14] Kwon et al. (2006), [15] Oya et al. (2018), [16] Choi et al. (2006), [17] Choi (2001), [18] Maury et al. (2019), [19] Bachiller et al. (1998), [20] Gaudel et al. (2020), [21] Tobin et al. (2011), [22] Wiseman et al. (2001), [23] Tanner & Arce (2011), [24] Saito et al. (1999), [25] Antonio Hernández-Gómez's PhD thesis, private communication. [26] Huang & Hirano (2013).

this respect, the N_2D^+ emission might better trace the gas kinematics in the envelope. The velocity map derived from the N_2D^+ datacube is presented in Fig. E.1. Using these data over a $30'' \times 30''$ region (equivalent to the $\pm 20''$ regions used for the Perseus sources), we obtain a weaker but still strong velocity gradient of $\sim 15 \text{ km s}^{-1} \text{ pc}^{-1}$. We chose to use this measurement in the remaining analysis.

B335. B335 is a particular case; very little rotation is observed in the source. Menten et al. (1984) only reported a velocity shift from NH_3 observations of a few $10^{-2} \text{ km s}^{-1}$ over half an arcmin scale, which was confirmed by the weak velocity gradient estimated by Caselli et al. (2002). Based on Saito et al. (1999) (their Fig 5), we derive a velocity gradient of $1 \text{ km s}^{-1} \text{ pc}^{-1}$ over the interval $\pm 60''$ (equivalent to the $\pm 20''$ regions used in Perseus) in the NS direction (i.e., perpendicular to the outflow). A recent study by Watson (2020), based on the reflection nebosity of a nearby star, suggests that the distance to B335 could be 165 pc (we use 100 pc in this study). This greater distance, although it does not affect the mean B-field position angle derived for the source much, would lead to a velocity gradient about a factor of 2 lower than we used in this analysis. We note that there is still much uncertainty in the position angle of the velocity gradient for this source; the C^{18}O velocity gradient is tilted by 18° with respect to the east-west outflow direction (Yen et al. 2015a,b).

We did not analyze the position angle of the velocity gradient for this source.

HH212 and IRAS16293-A. The remaining velocity gradients were directly taken from the literature or were obtained from private communication. For HH212, Wiseman et al. (2001) determined a velocity gradient of about $4\text{--}5 \text{ km s}^{-1} \text{ pc}^{-1}$ over a $25\text{--}30''$ region. For IRAS16293, the gradient calculated from the H^{13}CO^+ velocity map of Rao et al. (2009) is huge ($430 \text{ km s}^{-1} \text{ pc}^{-1}$) and covers the whole IRAS16293-A/IRAS16293-B system. ALMA and SMA are both observing this large velocity gradient that might be partly contaminated by the various outflows emerging from this complex system. When CN observations are used (Antonio Hernández-Gómez's PhD thesis³, private communication), then the velocity gradient observed perpendicular to the main EW outflow decreases to $25 \text{ km s}^{-1} \text{ pc}^{-1}$. We use this value in the paper.

HH25-MMS and HH797. Finally, we were unable to find observations for HH25 that would allow us to estimate a velocity

³ <https://tel.archives-ouvertes.fr/tel-02492210/>

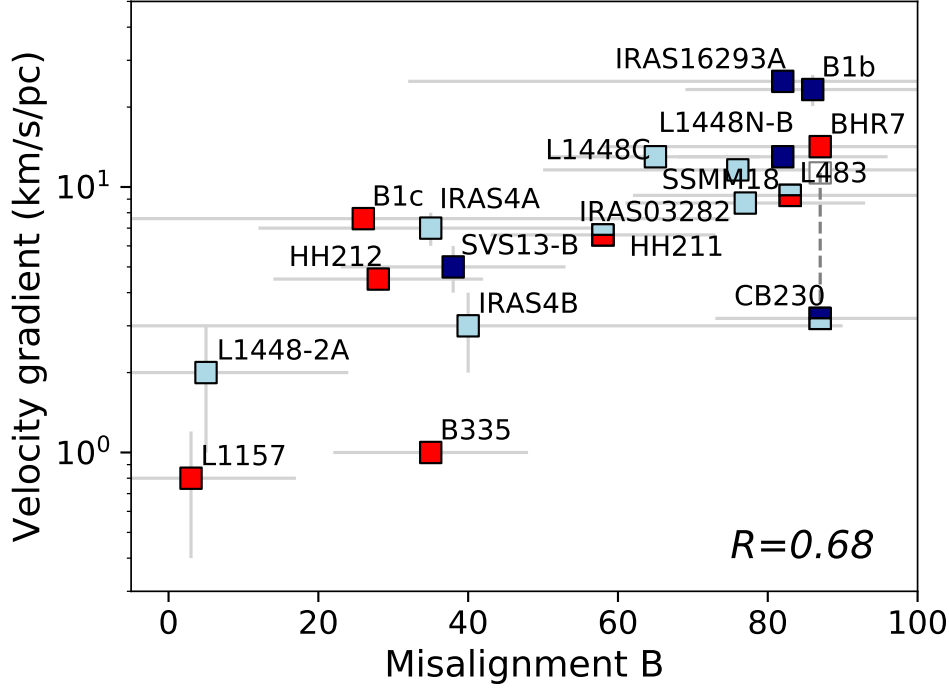


Fig. 3. Projected angle between the mean magnetic field within the 1000 au central region and the outflow direction as a function of the velocity gradient of the source estimated from line measurements. Sources are color-coded as a function of their fragmentation below 5000 au scales (with red, light blue, and dark blue for sources with a detection of a single, double, and 3-4 dust peaks). For certain sources, two colors are used: For L483, the ALMA 1.2 mm map from Oya et al. (2017) revealed a continuum source detected at a 5σ level in the south-west region that might suggest fragmentation. For HH211, Lee et al. (2009) detected a companion source with the SMA in the southwestern extension of the source, but VLA and ALMA observations have questioned the binary nature of the source (Tobin et al. 2016; Lee et al. 2019). In both cases, the nature of the additional source needs to be better investigated to be confirmed or refuted as a companion. Finally, the companion to CB230-A appears to host two near-IR objects, thus could be part of a triple system (Massi et al. 2008). For this source, we also indicate both the velocity gradient derived by Tobin et al. (2011) from a 1D fit perpendicular to the outflow direction (empty symbol) and a 2D fit of the total velocity field (filled symbol) because the two measurements lead to different values of the velocity gradient.

gradient. Although it is located in the window of observations, the H^{13}CO^+ line is unfortunately not detected in this object by SMA. For HH797, the complex velocity pattern derived from the C^{18}O datacube from Palau et al. (2014) did not allow us to estimate a clean velocity gradient strength or direction. We decided to drop these two sources for the remaining analysis.

The velocity gradient strengths (in $\text{km s}^{-1} \text{pc}^{-1}$) and position angles used in this analysis are summarized in Table 4. The bulk of the velocity gradients resides in the $[0-20] \text{ km s}^{-1} \text{pc}^{-1}$ range. This range is consistent with that derived for a sample of 17 nearby protostellar systems by Tobin et al. (2011) (their Fig. 26 right). We note that velocity gradients aligned in the equatorial plane are commonly interpreted as envelope rotation. Recent analyses have revealed a more complex interpretation, with sources showing shifts or even reversal of the gas velocity gradients within envelopes. In some sources, the observed gradients might even originate from ongoing infall or be linked with turbulence (Gaudel et al. 2020). In all cases, however, large velocity gradients trace more dynamical envelopes with higher kinetic energy.

4. Discussion

4.1. Misaligned B fields associated with the small angular momentum of the protostellar gas

Galametz et al. (2018) qualitatively noted a higher occurrence of misaligned B-field lines in sources in which large velocity gradients were detected in the equatorial plane at scales of thousands of au. The measurements of the envelope kinematics combined with B position angle measurements allow us to quantify the relation. In Fig. 3 we show the projected angle between the B-field orientation and the outflow axis as a function of the velocity gradient (in $\text{km s}^{-1} \text{pc}^{-1}$) that we used as a proxy to probe the gas dynamics in the surrounding envelope. Errors on the misalignment angles (x-axis) are the addition of the B-field orientation error quoted in Table 4 and that of the outflow position angle error. The colors used in the plot are discussed in § 4.2.

We observe a reasonably good ($R=0.68$) positive correlation between the misalignment of B with respect to the outflow and the strength of the velocity gradient traced at envelope scales. This quantitatively demonstrates that a relation exists between the orientation of the magnetic field and the kinematic energy in envelopes. This is consistent with the result presented in Yen et al. (2015a) and based on a sample of 17 Class 0 and I protostars where no source with large specific angular momenta were found with a strongly aligned configuration. The

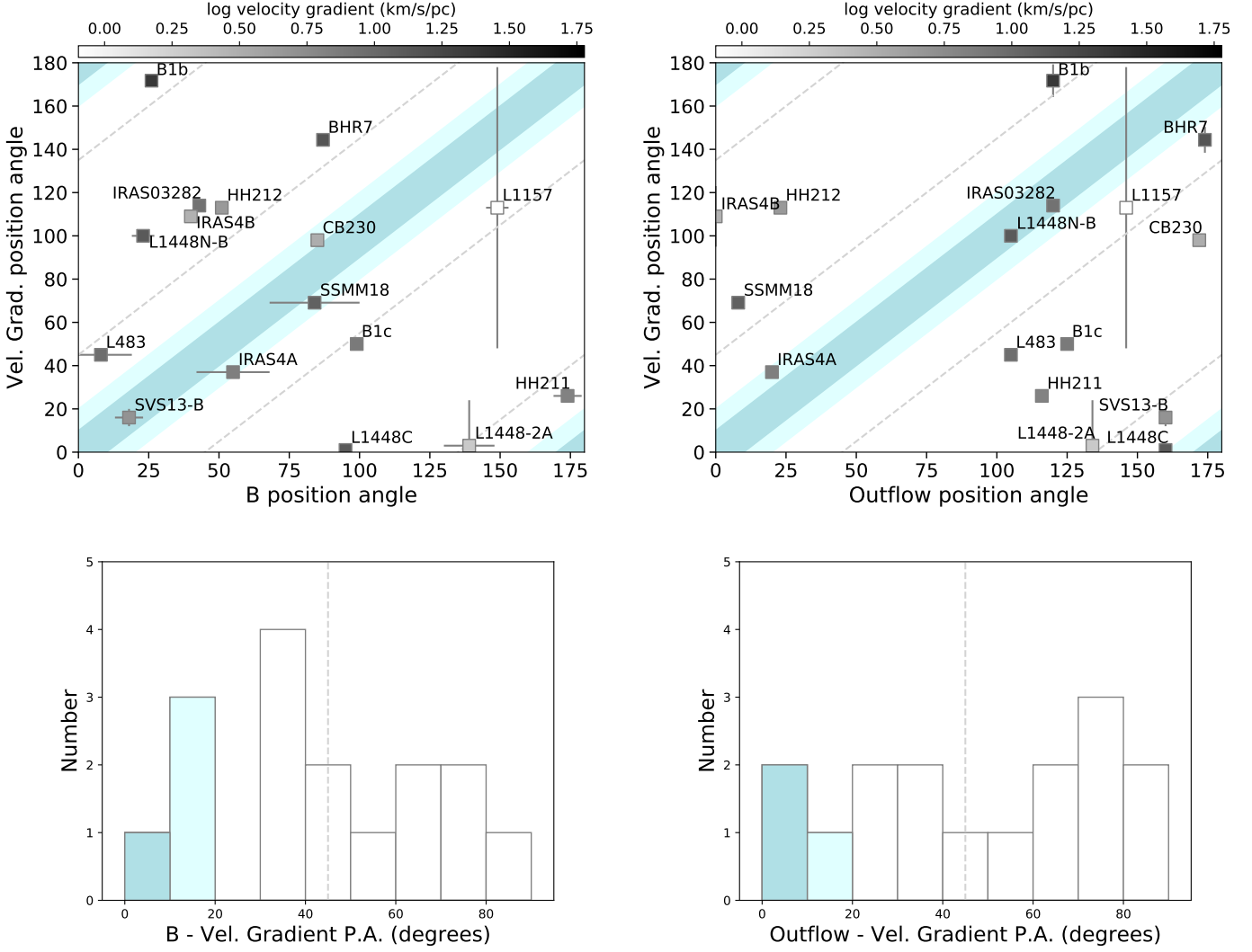


Fig. 4. *Top left:* Velocity gradient position angle as a function of the mean magnetic field position angle. The light and darker blue stripes indicate a projected angle between the two smaller than 20° and 10° , respectively. The dashed line indicates a difference of 45° between the two position angles. Protostars are color-coded as a function of their velocity gradient, with increasing gradients as the color darkens. *Top right:* Relation between the velocity gradient position angle and the outflow direction. We use the same convention for the stripes and lines. We note that the blue regions indicate sources whose velocity gradient might partly be tracing the outflow motion rather than the envelope motions. *Bottom:* Corresponding histograms of the misalignment of (left) the B field and (right) the outflow axis with respect to the velocity gradient position angle. Colors and lines delineate the same angle offsets as in the top panels.

correlation observed in Fig. 3 may be interpreted in various ways. One interpretation might be that the misalignments of B at envelope scales are driven by the strong rotational or infall motions of the envelope, while another interpretation might be that an aligned B field could have favored the smaller velocity gradients we observe.

If the misalignment of B with respect to the outflow at envelope scales were driven by the envelope kinematics (i.e., if the initially aligned B-field lines were to be twisted by the infalling or rotating matter), we would expect a relation of the position angle of B and that of the velocity gradient. We plot the velocity gradient position angle as a function of the mean magnetic field position angle in Fig. 4 (left). To facilitate visualization, the light and darker stripes indicate where the projected angle between the two directions is smaller than 20° and 10° , respectively. The

dashed line indicates a difference of 45° between the two position angles. We color-code sources as a function of the velocity gradient strength. The bottom left panel shows the corresponding histogram of the angular difference between the position angle of B and the velocity gradient position angle.

We observe that regardless of the height (so potentially effect) of the velocity gradient, we do not observe an alignment of the magnetic field direction and the velocity gradient position angle. This suggests that the B-field lines do not preferentially follow the direction of the matter infall and collapse dynamics. On the contrary, the sources seem to be scattered across the plot, as highlighted by the relatively flat corresponding histogram (Fig. 4 bottom left). This could indicate that the correlation observed in Fig. 3 has a more complex explanation than matter infall or rotation that causes the misaligned magnetic field lines. This could favor the second interpretation, namely that in

sources showing an aligned configuration of B, magnetic braking could be more efficient at removing angular momentum, leading to the smaller velocity gradient we observe.

Reinforcing the interpretation that the correlation may be due to more efficient magnetic braking at removing angular momentum in sources initially in an aligned configuration of B further, we stress that most sources with low values of their envelope gas velocity gradient also have an envelope B field that is well aligned with the field observed in their surrounding environment. The large-scale magnetic field lines probed around L1157 by Planck or probed at intermediate scales with SHARP (Stephens et al. 2013; Chapman et al. 2013) are consistent with the SMA B orientation. We note that results from optical polarimetry are also consistent, with a small angle offset $<20^\circ$ (Sharma et al. 2020). For B335, the orientation of the near-IR polarization vectors seems to also fit with the orientation of the submillimeter polarization vectors (Bertrang et al. 2014) and with the east-west direction found with JCMT-POL by Yen et al. (2019). Finally, the B-field lines in NGC 1333 IRAS4A, HH211, or L1448-2A appear to be extremely well ordered at scales traced by the SHARP or SCUBA instruments (Hull et al. 2014, see) down to the SMA scales. B1-c does not follow this trend, however, with a large-scale B field oriented with a position angle of 35° (Matthews & Wilson 2002), that is, nearly perpendicular to the outflow direction, compared to the SMA 100° orientation.

The nature of the gas kinematics recovered at these envelope scales (i.e., whether the angular momentum originates from rotation, infall, or even from turbulent motions inherited from the initial conditions and/or turbulence), is unknown. Its amount appears to be intimately linked to the magnetic configuration in protostellar envelopes, however.

4.2. Indication of higher multiplicity in systems with misaligned magnetic fields ?

In order to investigate the effect of the magnetic field on the envelope fragmentation, we color-code the sources of Fig. 3 depending on whether they are fragmented below 5000 au scales. We indicate in particular whether the source hosts a single, double, triple, or quadruple dust peak (using submillimeter direct imaging). Details of the fragmentation for each individual source are provided in Appendix A. We stress that very close multiplicity (below 100 au scales) is not considered in our analysis.

We observe that sources standing as single objects (in red) mostly appear to reside in the bottom left corner of the plot, that is, with relatively small velocity gradients of their surrounding envelopes and aligned magnetic field orientation with respect to the outflow axis. Uncertainties also remain about the nature of potential companions detected in HH211 and L483, hence these sources appear with two colors in Fig. 3. In order to assess whether the two populations (single versus multiple) belong to the same distribution, we applied a 2D Kolmogorov-Smirnov test. We used the two python scripts *ndtest.py*⁴ and *KS2D.py*⁵ to estimate the K-S statistics and p-values. These 2D testings are based on statistical methods developed by Peacock (1983) and Fasano & Franceschini (1987). Excluding the sources for which the exact multiplicity nature is unsure (i.e., HH211 and L483), both methods return the same low p-value of 0.13, indicating that the single and multiple source populations likely do not belong to the same population. More sources would, however, be necessary to reinforce this statistical test. We also note that

the two sources SVS13-B and IRAS4B have large-scale companions (SVS13-A and IRAS4B2 located at 4200 au and 3200 au from SVS13-B and IRAS4B1, respectively), but they do not seem to be fragmented below 3000 au scales, to our knowledge. These sources have moderate velocity gradients and B is misaligned, so they are both located in the bottom left quadrant of Fig. 3. When our separation criterion is whether fragmentation is observed above and below 3000 au scales (compared to 5000 au scales as before), the p-value of the previous K-S test drops to 0.04, which is also consistent with our conclusion that a dichotomy exists between the single versus multiple source population and that the magnetic field alignment might affect the way in which the envelope fragments.

Observational studies have suggested that the magnetic field might affect the fragmentation rate at molecular clouds or filaments scales (e.g., Teixeira et al. 2016; Koch et al. 2018). Our analysis at protostellar envelope scales appears to support the theoretical predictions that the magnetic field orientation in the envelope also plays a role in favoring or inhibiting the fragmentation processes of a dense protostellar core into multiple systems. We further discuss the predictions from MHD simulations and their relation to our results in the following section.

4.3. Consistency with predictions from MHD simulations

In ideal MHD models, B fields are shown to strongly regulate the transport of angular momentum and hence modify the final properties of stars and disks (see Hennebelle & Inutsuka 2019; Wurster & Li 2018; Zhao et al. 2020, and references therein). The inclusion of more realistic non-ideal MHD effects changed this view, with finer effects that may play a crucial role regarding the ability of B to interact with gas kinematics, such as ionization and dust properties (Zhao et al. 2018). Some studies have shown that B is in particular less efficient at transporting angular momentum when it is initially misaligned with the rotation of the system (Joos et al. 2012).

That a link might exist between the initial core-scale magnetic field orientation with respect to the rotation axis that drives the small-scale outflow launching and fragmentation has been predicted by models of protostellar formation. Through the collapse of a dense rotating infalling core and in the extreme case of an envelope rotation axis initially perpendicular to the magnetic field, Price & Bate (2007) have shown, for instance, that the magnetic tension appears to play an even more significant role in helping fragmentation. Inserting magnetic fields also appears to be a necessary condition to reproduce the fragmentation rates now observed in massive cores with ALMA, as suggested by Fontani et al. (2016). The observations provide information of the main field direction at envelope scales: in an aligned configuration, thus more organized magnetic field configuration, the magnetic pressure will be more efficient at stabilizing the envelope, reducing the rotation-induced fragmentation at comparable scales (i.e., below 5000 au scales). If fragmentation were favored by less efficient magnetic braking processes, it could also be enhanced by ‘turbulent’ fragmentation, that is, fragmentation linked to the increase of the kinematic energy of envelopes in misaligned configurations. Following our observational results, a study of non-ideal MHD models of protostellar collapse that searched for the roots of the correlation we report was initiated and is currently carried out by the team.

The question is whether a potential effect of the misaligned B-field orientation on the final protostellar disk sizes might be observed. If less angular momentum is transported from the en-

⁴ <https://github.com/syrte/ndtest/blob/master/ndtest.py>

⁵ <https://github.com/Gabinou/2DKS/blob/master/KS2D.py>

velope to the disk scales in the case of B-aligned configuration, as suggested by our study at envelope scales, smaller rotation-supported disks are expected. Observationally, the small size of disks in some Class 0 protostars has been interpreted as a consequence of an efficient magnetic braking that potentially disrupts the disk formation (Maury et al. 2010; Yen et al. 2015a; Segura-Cox et al. 2018). Magnetohydrodynamics simulations from Hirano et al. (2020) recently confirmed that in the later accretion phase, the smallest disk radius and mass are produced in alignment-configuration cases. Using the CALYPSO sample, Maury et al. (2019) have shown that fewer than 25% of the 26 Class 0 protostars may harbor large protostellar disks resolved at radii >60 au. Their results also favor a magnetized scenario for the disk formation. Unfortunately, most sources with large disk-like structures (L1527, SMM4, MM22, and GF9-2) are not included in the current sample. The disk sizes are mostly unresolved at ~ 50 au scales in the remaining sources of our sample that overlap with the CALYPSO sample. This prevents us from studying the effect of the B misalignment on the disk formation itself. Such studies are currently hampered by the need of very high spatial resolution to study these disks with ALMA, for instance. Recent ALMA results from Cox et al. (2018) have analyzed, for instance, the polarization angle dispersion and tried to connect the signature or randomness of the B field with the disk or non-disk nature of their sources. The extremely complex morphology of magnetic fields in Class 0 protostars observed with ALMA at 50 au typical disk scales may suggest a less dynamically relevant B field at these scales, as expected from non-ideal MHD models (e.g., with ambipolar diffusion leading to a weaker coupling of the magnetic field lines with the circumstellar gas; Mellon & Li 2009; Tsukamoto et al. 2015). We stress, however, that the characterization of B in disks remains problematic, as several mechanisms can contribute to the production of polarized dust emission at these scales (Kataoka et al. 2015; Cox et al. 2018).

4.4. Assessing the various caveats

4.4.1. Outflow contamination

Assessing the preferential direction and strength of the moving gas in protostellar envelopes is complicated by the presence of outflows (sometimes more than one, e.g., in the case of IRAS16293-A) that can contribute to the observed gradients, although our choice of mostly using a dense or cold gas tracer such as N_2H^+ should largely limit the contamination. In Fig. 4 (right) we plot the velocity gradient position angle as a function of the outflow direction. The dashed line delineates a difference of 45° between the two position angles. The light and darker stripes indicate when the projected angle between the two is smaller than 20° and 10° , respectively, which indicates regions with sources whose velocity gradient might be more related to the outflow dynamics than to the envelope kinematics we analyzed here. The bottom right panel of Fig. 4 provides the histogram of the misalignment of the outflow and the gradient. The dispersion in the outflow - gradient misalignment is consistent with the results from Tobin et al. (2011) (their Fig. 27). For only 3 sources is the velocity gradient roughly aligned with the outflow direction, that is, with $\Delta(\text{P.A.}) < 30^\circ$ (see Fig. 4 right).

4.4.2. Projection effects

The position and misalignment angles quoted in this analysis are projected in the plane of the sky and might differ from the real

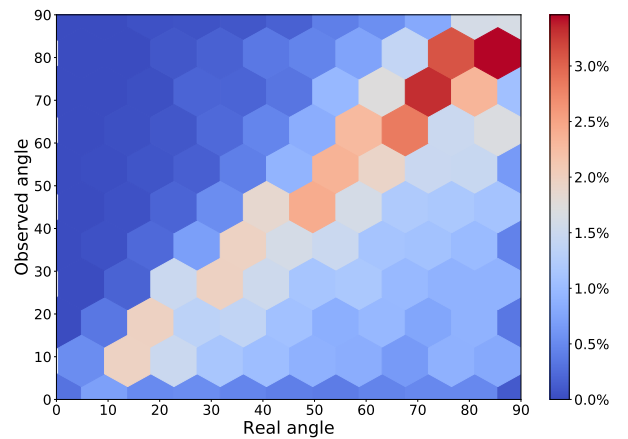


Fig. 5. Monte Carlo test for 10000 randomly generated vector pairs projected onto a 3D plane mimicking the plane of the sky. This plot shows the density distribution of the angles obtained by projecting these vector pairs onto the plane compared to their real angle separation in 3D. The color bar indicates the probabilities of each projected vs. true angle pair.

angles between the various directions analyzed (velocity gradients, B, and outflows). In order to assess the uncertainties linked with projection effects, we performed a Monte Carlo test. We developed a python script that randomly generates a 3D plane. This plane was our plane of the sky. We then generated 10000 random pairs of vectors in this 3D space. For each pair, vectors were projected onto the 3D plane (using the orthogonal basis of the plane) to estimate the two ‘projected vectors’ and thus ‘observed angle’ between the two. The ‘real’ and ‘observed’ angles were then compared. Figure 5 shows the density distribution of the observed versus real angles. The 2D density plot is generated with the *hexbin* python function (Seaborn package). For simplicity, we modified the color bar to indicate the probabilities of each observed-real angle pair. As expected, the projected angles are most of the time equal to (i.e., on the diagonal) or lower (i.e., on the bottom right area) than the corresponding real angle. Qualitatively, the bright diagonal highlights that we did not make a fundamental mistake by taking the observed angle as a proxy for the real angle.

To quantify the effects, we separated the ‘observed’ angles into 18 bins of 5° each and provide the mean ‘real angle’ in Table 5. The standard deviations for each observed angle bins are provided as uncertainties. We note that the ‘true angle’ distributions corresponding to each bin are not Gaussian. We observe that the largest discrepancies between the ‘real’ and ‘observed’ angles appear for ‘observed’ angles below 40° , with large error bars. In Fig. 3, these projection effects could therefore shift the sources with a B misalignment lower than 40° to the right and realign these sources along a more global linear correlation because the projection effects do not strongly affect sources beyond a 40° misalignment. Synthetic observations derived from MHD simulations are currently developed by the team to complement these tests on projection effects (Valdivia et al. in prep.).

4.4.3. Dependence on tracers

One of the caveats of this analysis is also that it depends on the molecular line tracers chosen. Both C^{18}O and N_2H^+ datacubes are available for the CALYPSO sources. We decided to select N_2H^+ as a tracer of the envelope kinematics. Several analyses

Table 5. Mean ‘true angle’ per ‘observed angle’ bins

| Observed angle (°) | Mean ‘true angle’ (°) |
|-----------------------|--------------------------|
| [0 - 5] | 38.8 ± 25.4 |
| [5 - 10] | 36.2 ± 25.3 |
| [10 - 15] | 41.3 ± 24.3 |
| [15 - 20] | 38.7 ± 22.5 |
| [20 - 25] | 41.4 ± 21.6 |
| [25 - 30] | 46.0 ± 19.7 |
| [30 - 35] | 48.3 ± 18.5 |
| [35 - 40] | 50.0 ± 18.8 |
| [40 - 45] | 52.4 ± 16.1 |
| [45 - 50] | 54.6 ± 16.3 |
| [50 - 55] | 60.5 ± 15.0 |
| [55 - 60] | 65.5 ± 14.6 |
| [60 - 65] | 65.4 ± 14.5 |
| [65 - 70] | 69.6 ± 14.0 |
| [70 - 75] | 73.4 ± 14.2 |
| [75 - 80] | 76.6 ± 14.4 |
| [80 - 85] | 79.1 ± 15.1 |
| [85 - 90] | 80.2 ± 14.5 |

have shown it to be a robust tracer of the outer envelopes, thus the scales we trace with the SMA, rather than of the central regions where this molecule is usually depleted and whose kinematics gas are then usually traced through $C^{18}O$ or H_2D^+ (Bergin et al. 2002; Anderl et al. 2016; Gaudel et al. 2020; Maret et al. 2020). We used the NH_3 molecule for HH212: the joined analysis of N_2H^+ and NH_3 by Tobin et al. (2011) has confirmed that both lines trace similar physical conditions at the scales we study here. We also selected N_2D^+ and CN as complementary tracers of cold dense gas. Thus, unless some strongly different chemical effects are at work in the different protostellar envelopes, all sources have been observed with homogeneous gas tracers. Variations in the opacity from one source to another could bias the physical scales at which the velocity gradients are probed, with the observed N_2H^+ arising from projected shells or more external regions than what we assumed. N_2H^+ or N_2D^+ could also be absent near the protostar, although this should not have a strong effect on the scales probed in this analysis. A more extended analysis using other tracers of the gas dynamics would help test the robustness of our conclusions at various envelope radii and/or for gas that is subject to different local conditions.

5. Summary

We have carried out dust polarization observations at 0.87 mm for 20 Class 0 protostars with the SMA. We analyzed the misalignment of the magnetic field orientation (derived over the central 1000 au scales) with the outflow orientation in order to compare this misalignment with the gas kinematics. The dynamics of the gas was traced through measurements of velocity gradients at envelope scales using molecular line emission. Our analysis provides for the first time a quantification of the striking correlation that links the misalignment of the magnetic field orientation at envelope scales and the angular momentum of the gas reservoir that is directly involved in the star formation process. Comparing the trend with the presence of multiple stellar systems, we also show that sources that tend to stand as single objects mostly reside in environments with a weak velocity gradient and/or a

rather aligned B-field orientation compared to the outflow axis. Altogether, the observations tend to show a coherent picture for the role of the magnetic field in forming stars and their protoplanetary disks: they suggest that strong B fields in an aligned configuration may be more efficient in regulating both the gas kinematics and the level of fragmentation during the early embedded phases of star and disk formation. Our findings could be in line with theoretical expectation from the most recent magnetized models of star formation, which predict reduced angular momentum at smaller scales due to magnetic braking, although a thorough exploration of the physical causes behind the observed correlations should be explored in numerical models. Our results provide a strong observational confirmation of the cornerstone role of B in regulating the formation of stellar systems and settling the primordial conditions from which the future disk, star, and planets will form.

Acknowledgments

We thank the anonymous referee for his/her constructive suggestions that improve our methodology descriptions and overall quality of the manuscript. This project has received funding from the European Research Council (ERC) under the European Union Horizon 2020 research and innovation programme (MagneticYSOs project, grant agreement N° 679937, PI: Maury). J.M.G. is supported by the grant AYA2017-84390-C2-R (AEI/FEDER, UE). We thank John Tobin for providing us with the BHR7 H_2CO and N_2D^+ datacubes (presented in Tobin et al. 2018). We also thank Naomi Hirano and Brenda Matthews for providing us with the N_2H^+ data cubes for B1b and B1c respectively (data presented in Huang & Hirano (2013) and Matthews et al. (2008)). We finally thank Aina Palau for providing us with the $C^{18}O$ data cube for HH797 (see Palau et al. 2014). This publication is based on data of the Submillimeter Array. The SMA is a joint project between the Smithsonian Astrophysical Observatory and the Academia Sinica Institute of Astronomy and Astrophysics, and is funded by the Smithsonian Institution and the Academia Sinica.

References

- Allen, A., Li, Z.-Y., & Shu, F. H. 2003, *ApJ*, 599, 363
Anderl, S., Maret, S., Cabrit, S., et al. 2016, *A&A*, 591, A3
Andersen, B. C., Stephens, I. W., Dunham, M. M., et al. 2019, *ApJ*, 873, 54
Andersson, B.-G., Lazarian, A., & Vaillancourt, J. E. 2015, *ARA&A*, 53, 501
André, P., Ward-Thompson, D., & Barsony, M. 2000, *Protostars and Planets IV*, 59
Anthony-Twarog, B. J. 1982, *AJ*, 87, 1213
Bachiller, R., Guilloteau, S., Gueth, F., et al. 1998, *A&A*, 339, L49
Bachiller, R., Pérez Gutiérrez, M., Kumar, M. S. N., & Tafalla, M. 2001, *A&A*, 372, 899
Bergin, E. A., Alves, J., Huard, T., & Lada, C. J. 2002, *ApJ*, 570, L101
Bertrang, G., Wolf, S., & Das, H. S. 2014, *A&A*, 565, A94
Bontemps, S., André, P., & Ward-Thompson, D. 1995, *A&A*, 297, 98
Caselli, P., Benson, P. J., Myers, P. C., & Tafalla, M. 2002, *ApJ*, 572, 238
Chapman, N. L., Davidson, J. A., Goldsmith, P. F., et al. 2013, *ApJ*, 770, 151
Chen, X., Arce, H. G., Zhang, Q., et al. 2013, *ApJ*, 768, 110
Choi, M. 2001, *ApJ*, 553, 219
Choi, M., Hodapp, K. W., Hayashi, M., et al. 2006, *ApJ*, 646, 1050
Ciardi, A. & Hennebelle, P. 2010, *MNRAS*, 409, L39
Codella, C., Cabrit, S., Gueth, F., et al. 2014, *A&A*, 568, L5
Coudé, S., Bastien, P., Houde, M., et al. 2019, *ApJ*, 877, 88
Cox, E. G., Harris, R. J., Looney, L. W., et al. 2018, *ApJ*, 855, 92
Duchêne, G. & Kraus, A. 2013, *Annual Review of Astronomy and Astrophysics*, 51, 269
Dunham, M. M., Arce, H. G., Mardones, D., et al. 2014, *ApJ*, 783, 29
Dutrey, A., Guilloteau, S., & Bachiller, R. 1997, *A&A*, 325, 758
Estalella, R. 2017, *PASP*, 129, 025003
Evans, II, N. J., Dunham, M. M., Jørgensen, J. K., et al. 2009, *ApJS*, 181, 321
Fasano, G. & Franceschini, A. 1987, *MNRAS*, 225, 155

- Fontani, F., Commerçon, B., Giannetti, A., et al. 2016, *A&A*, 593, L14
- Galametz, M., Maury, A., Girart, J. M., et al. 2018, *A&A*, 616, A139
- Galli, D., Lizano, S., Shu, F. H., & Allen, A. 2006, *ApJ*, 647, 374
- Gaudel, M., Maury, A. J., Belloche, A., et al. 2020, *A&A*, 637, A92
- Gerin, M., Pety, J., Commerçon, B., et al. 2017, *A&A*, 606, A35
- Gerin, M., Pety, J., Fuente, A., et al. 2015, *A&A*, 577, L2
- Gibb, A. G. & Davis, C. J. 1998, *MNRAS*, 298, 644
- Girart, J. M., Estalella, R., Palau, A., Torrelles, J. M., & Rao, R. 2014, *ApJ*, 780, L11
- Girart, J. M., Rao, R., & Marrone, D. P. 2006, *Science*, 313, 812
- Goodman, A. A., Benson, P. J., Fuller, G. A., & Myers, P. C. 1993, *ApJ*, 406, 528
- Gray, W. J., McKee, C. F., & Klein, R. I. 2018, *MNRAS*, 473, 2124
- Gueth, F. & Guilloteau, S. 1999, *A&A*, 343, 571
- Hatchell, J., Fuller, G. A., & Richer, J. S. 2007, *A&A*, 472, 187
- Hennebelle, P., Commerçon, B., Chabrier, G., & Marchand, P. 2016, *ApJ*, 830, L8
- Hennebelle, P., Commerçon, B., Lee, Y.-N., & Charnoz, S. 2020, *A&A*, 635, A67
- Hennebelle, P. & Fromang, S. 2008, *A&A*, 477, 9
- Hennebelle, P. & Inutsuka, S.-i. 2019, *Frontiers in Astronomy and Space Sciences*, 6, 5
- Hennebelle, P. & Teyssier, R. 2008, *A&A*, 477, 25
- Herczeg, G. J., Kuhn, M. A., Zhou, X., et al. 2019, *ApJ*, 878, 111
- Hirano, N., Kamazaki, T., Mikami, H., Ohashi, N., & Umemoto, T. 1999, in *Star Formation 1999*, ed. T. Nakamoto, 181–182
- Hirano, N., Kameya, O., Nakayama, M., & Takakubo, K. 1988, *ApJ*, 327, L69
- Hirano, S. & Machida, M. N. 2019, *MNRAS*, 485, 4667
- Hirano, S., Tsukamoto, Y., Basu, S., & Machida, M. N. 2020, *arXiv e-prints*, arXiv:2006.13233
- Hsu, D. C., Ford, E. B., Ragozzine, D., & Ashby, K. 2019, *AJ*, 158, 109
- Huang, Y.-H. & Hirano, N. 2013, *ApJ*, 766, 131
- Hull, C. L. H., Plambeck, R. L., Bolatto, A. D., et al. 2013, *ApJ*, 768, 159
- Hull, C. L. H., Plambeck, R. L., Kwon, W., et al. 2014, *ApJS*, 213, 13
- Hull, C. L. H. & Zhang, Q. 2019, *Frontiers in Astronomy and Space Sciences*, 6, 3
- Joos, M., Hennebelle, P., & Ciardi, A. 2012, *A&A*, 543, A128
- Jørgensen, J. K. 2004, *A&A*, 424, 589
- Kataoka, A., Muto, T., Momose, M., et al. 2015, *ApJ*, 809, 78
- Koch, P. M., Tang, Y.-W., Chapman, N. L., et al. 2018, *arXiv e-prints*, arXiv:1801.06995
- Kwon, W., Looney, L. W., Crutcher, R. M., & Kirk, J. M. 2006, *ApJ*, 653, 1358
- Kwon, W., Stephens, I. W., Tobin, J. J., et al. 2019, *ApJ*, 879, 25
- Launhardt, R., Stutz, A. M., Schmiedeke, A., et al. 2013, *A&A*, 551, A98
- Le Gouellec, V. J. M., Hull, C. L. H., Maury, A. J., et al. 2019, *ApJ*, 885, 106
- Lee, C.-F., Hasegawa, T. I., Hirano, N., et al. 2010, *ApJ*, 713, 731
- Lee, C.-F., Hirano, N., Palau, A., et al. 2009, *ApJ*, 699, 1584
- Lee, C.-F., Ho, P. T. P., Bourke, T. L., et al. 2008, *ApJ*, 685, 1026
- Lee, C.-F., Kwon, W., Jhan, K.-S., et al. 2019, *ApJ*, 879, 101
- Lee, C.-F., Li, Z.-Y., Ching, T.-C., Lai, S.-P., & Yang, H. 2018, *ApJ*, 854, 56
- Lee, C.-F., Rao, R., Ching, T.-C., et al. 2014, *ApJ*, 797, L9
- Lee, J. W. Y., Hull, C. L. H., & Offner, S. S. R. 2017, *ApJ*, 834, 201
- Li, H., Griffin, G. S., Krejny, M., et al. 2006, *ApJ*, 648, 340
- Marcelino, N., Gerin, M., Cernicharo, J., et al. 2018, *A&A*, 620, A80
- Maret, S., Maury, A. J., Belloche, A., et al. 2020, *A&A*, 635, A15
- Marrone, D. P. 2006, PhD thesis, Harvard University
- Marrone, D. P. & Rao, R. 2008, in *Proc. SPIE*, Vol. 7020, Millimeter and Submillimeter Detectors and Instrumentation for Astronomy IV, 70202B
- Massi, F., Codella, C., Brand, J., di Fabrizio, L., & Wouterloot, J. G. A. 2008, *A&A*, 490, 1079
- Masson, J., Chabrier, G., Hennebelle, P., Vaytet, N., & Commerçon, B. 2016, *A&A*, 587, A32
- Mathews, B., Bergin, E., Crapsi, A., et al. 2008, *Ap&SS*, 313, 65
- Mathews, B. C., Hogerheijde, M. R., Jørgensen, J. K., & Bergin, E. A. 2006, *ApJ*, 652, 1374
- Mathews, B. C., McPhee, C. A., Fissel, L. M., & Curran, R. L. 2009, *ApJS*, 182, 143
- Mathews, B. C. & Wilson, C. D. 2002, *ApJ*, 574, 822
- Maury, A. J., André, P., Hennebelle, P., et al. 2010, *A&A*, 512, A40+
- Maury, A. J., André, P., Men'shchikov, A., Könyves, V., & Bontemps, S. 2011, *A&A*, 535, A77
- Maury, A. J., André, P., Testi, L., et al. 2019, *A&A*, 621, A76
- Maury, A. J., Girart, J. M., Zhang, Q., et al. 2018, *MNRAS*, 477, 2760
- Mellon, R. R. & Li, Z.-Y. 2009, *ApJ*, 698, 922
- Menten, K. M., Walmsley, C. M., Kruegel, E., & Ungerechts, H. 1984, *A&A*, 137, 108
- Olofsson, S. & Olofsson, G. 2009, *A&A*, 498, 455
- Ortiz-León, G. N., Loinard, L., Dzib, S. A., et al. 2018a, *ApJ*, 865, 73
- Ortiz-León, G. N., Loinard, L., Dzib, S. A., et al. 2018b, *ApJ*, 869, L33
- Oya, Y., Sakai, N., Watanabe, Y., et al. 2017, *ApJ*, 837, 174
- Oya, Y., Sakai, N., Watanabe, Y., et al. 2018, *ApJ*, 863, 72
- Palau, A., Zapata, L. A., Rodríguez, L. F., et al. 2014, *MNRAS*, 444, 833
- Park, Y. S., Panis, J. F., Ohashi, N., Choi, M., & Minh, Y. C. 2000, *ApJ*, 542, 344
- Peacock, J. A. 1983, *MNRAS*, 202, 615
- Plunkett, A. L., Fernández-López, M., Arce, H. G., et al. 2018, *A&A*, 615, A9
- Price, D. J. & Bate, M. R. 2007, *MNRAS*, 377, 77
- Rao, R., Girart, J. M., Marrone, D. P., Lai, S.-P., & Schnee, S. 2009, *ApJ*, 707, 921
- Sadavoy, S. I., Di Francesco, J., Andre, P., et al. 2014, *ApJ*, 787, L18
- Saito, M., Sunada, K., Kawabe, R., Kitamura, Y., & Hirano, N. 1999, *ApJ*, 518, 334
- Sault, R. J., Teuben, P. J., & Wright, M. C. H. 1995, in *Astronomical Society of the Pacific Conference Series*, Vol. 77, *Astronomical Data Analysis Software and Systems IV*, ed. R. A. Shaw, H. E. Payne, & J. J. E. Hayes, 433
- Segura-Cox, D. M., Looney, L. W., Tobin, J. J., et al. 2018, *ApJ*, 866, 161
- Sharma, E., Gopinathan, M., Soam, A., et al. 2020, *A&A*, 639, A133
- Stephens, I. W., Looney, L. W., Kwon, W., et al. 2013, *ApJ*, 769, L15
- Stutz, A. M., Rubin, M., Werner, M. W., et al. 2008, *ApJ*, 687, 389
- Sugitani, K., Nakamura, F., Watanabe, M., et al. 2011, *ApJ*, 734, 63
- Tafalla, M., Kumar, M. S. N., & Bachiller, R. 2006, *A&A*, 456, 179
- Tanner, J. D. & Arce, H. G. 2011, *ApJ*, 726, 40
- Teixeira, P. S., Takahashi, S., Zapata, L. A., & Ho, P. T. P. 2016, *A&A*, 587, A47
- Terebey, S., Shu, F., & Cassen, P. 1984, *ApJ*, 286, 529
- Tobin, J. J., Bos, S. P., Dunham, M. M., Bourke, T. L., & van der Marel, N. 2018, *ApJ*, 856, 164
- Tobin, J. J., Hartmann, L., Chiang, H.-F., et al. 2011, *ApJ*, 740, 45
- Tobin, J. J., Looney, L. W., Li, Z.-Y., et al. 2016, *ApJ*, 818, 73
- Tobin, J. J., Sheehan, P. D., Megeath, S. T., et al. 2020, *ApJ*, 890, 130
- Tsukamoto, Y., Iwasaki, K., Okuzumi, S., Machida, M. N., & Inutsuka, S. 2015, *MNRAS*, 452, 278
- Vallée, J. P. 2004, *New Astronomy Reviews*, 48, 763
- Cernis, K. & Straizys, V. 2003, *Baltic Astronomy*, 12, 301
- Watson, D. M. 2020, *Research Notes of the American Astronomical Society*, 4, 88
- Wiseman, J., Wootten, A., Zinnecker, H., & McCaughrean, M. 2001, *ApJ*, 550, L87
- Woermann, B., Gaylard, M. J., & Otrupcek, R. 2001, *MNRAS*, 325, 1213
- Wurster, J. & Bate, M. R. 2019, *MNRAS*, 486, 2587
- Wurster, J. & Lewis, B. T. 2020, *MNRAS*, 495, 3807
- Wurster, J. & Li, Z.-Y. 2018, *Frontiers in Astronomy and Space Sciences*, 5, 39
- Yen, H.-W., Koch, P. M., Takakuwa, S., et al. 2015a, *ApJ*, 799, 193
- Yen, H.-W., Takakuwa, S., Koch, P. M., et al. 2015b, *ApJ*, 812, 129
- Yen, H.-W., Zhao, B., Hsieh, I. T., et al. 2019, *ApJ*, 871, 243
- Zhang, Q., Qiu, K., Girart, J. M., et al. 2014, *ApJ*, 792, 116
- Zhao, B., Caselli, P., Li, Z.-Y., & Krasnopolsky, R. 2018, *MNRAS*, 473, 4868
- Zhao, B., Tomida, K., Hennebelle, P., et al. 2020, *Space Sci. Rev.*, 216, 43
- Zucker, C., Speagle, J. S., Schlafly, E. F., et al. 2019, *ApJ*, 879, 125

Appendix A: Individual source characteristics

B1-bS

Continuum morphology at 850 μm . When the large-scale envelope of Per B1-b is elongated in the north-south direction and encompasses the two sources B1-bN and B1-bS (Chen et al. 2013), our SMA observations only focus on B1-bS. They reveal a core elongated in the northwest-southeast direction at 1000–2000 au scales, a morphology very similar to that observed at 3mm with the Nobeyama Array (Hirano et al. 1999) or 850 μm with ALMA (Gerin et al. 2017).

Fragmentation. The two submillimeter sources in B1-b were first discovered by Hirano et al. (1999). The companion of B1-bS is called B1-bN and is located $\sim 16''$ north. It was studied with the VLA by Tobin et al. (2016). The observations allowed them to show that the two sources have similar temperatures, but that B1-bS is twice as luminous as B1-bN. Both sources seem to be extremely different in terms of their richness in complex organic molecules (COM), as revealed by recent ALMA observations (Marcelino et al. 2018). The ALMA results do not reveal further fragmentation in B1-bS below 200 au scales. The

source Per-emb-41, located only 13'' in the southwest of B1-bS, appears to be more evolved (Tobin et al. 2016). *f Magnetic field orientation.* On the large scales observed by SCUBA (Matthews & Wilson 2002) or the B-fields In STar-forming Region Observations (BISTRO) survey (Coudé et al. 2019), the B1-b system already shows strong variations in its polarization position angle, with a mean value of the magnetic field direction position angle toward B1-bS of about 30°. This orientation is consistent with the average B-field orientation obtained with the SMA in the northeast region (26°). The western vectors are oriented at 111°, that is, perpendicular to the eastern vector and along the outflow direction. We decided to use the average northeast value for this analysis because it appears to trace the magnetic field better at envelope scales connected with the magnetic field traced on larger scales.

B1-c

Continuum morphology at 850 μm . The large-scale 2.7 and 3.3 mm continuum emission observed by Matthews et al. (2006) presents extensions mostly along the outflow. In contrast, the 850 μm SMA continuum is flattened in the direction perpendicular to the source outflow. This is consistent with the SMA 1.3 mm dust continuum image presented in Chen et al. (2013). The northern and southwestern plumes are also observed with ALMA at 870 μm (see Cox et al. 2018).

Fragmentation. The source is a single source at the SMA scales (this work), at the VLA scales probed by the VLA/ALMA Nascent Disk and Multiplicity (VANDAM) survey (Tobin et al. 2016), and at the ALMA scales probed by Cox et al. (2018).

Magnetic field orientation. At the large scales observed by SCUBA (Matthews & Wilson 2002), B1-c has a polarization angle at 35°, that is, a magnetic field nearly perpendicular to the outflow direction (estimated at -55°; Matthews et al. 2006). Matthews et al. (2008) and the results from the BISTRO survey (Coudé et al. 2019) revealed a more complex pattern. Our SMA results are consistent with these more recent results: the SMA northern vectors are oriented at an angle of 152° and the central vectors are oriented in an east-west orientation, with an average in position angle of 70°. The average in the central 1000 au region is 99°. Our results suggest that the hourglass configuration of the field lines observed with ALMA by Cox et al. (2018) already starts to be resolved at SMA scales.

BHR7-MMS

Continuum morphology at 850 μm . The SMA 850 μm continuum emission is elongated in the north-south direction. By comparison, the SMA 1.3 mm continuum emission presented in Tobin et al. (2018) is much more compact and marginally extended in the east-west direction, but was observed with the Very Extended Configuration, which has a resolution that is three to four times higher than that of the current analysis.

Fragmentation. BHR7-MMS is an isolated dark cloud. The source does not seem to be fragmented at the intermediate scales probed with the SMA (Tobin et al. 2018, and this work). Recently taken but not yet published ALMA observations of the source should reveal the inner morphology of the source in the coming years.

Magnetic field orientation. To our knowledge, this is the first time that polarized dust emission is used to probe the magnetic field direction in this source. We observe that B is oriented east-west, perpendicular to the direction of the outflow. The northern and southern vectors are slightly tilted compared to

the orientation of the central detection, which might be the signature of an hourglass morphology.

HH25-MMS

Continuum morphology at 850 μm . HH25-MMS is part of a string of embedded young stellar objects (the HH24-26 complex; Bontemps et al. 1995; Gibb & Davis 1998). SMA 870 μm observations by Chen et al. (2013) have shown that three distinct sources compose the system (SMM1, SMM2, and SMM3) and are aligned in the north-south direction. If SMM1 were the driving source of the HH25 outflow, the SMA polarization data focus on the SMM2 source. Its SMA continuum appears to be extended in the east-west direction.

Fragmentation. As mentioned previously, SMM2 is part of a three-source system, with separations of 13 and 11'' with SMM1 and SMM3, respectively. On larger scales, HH25-MMS also has a Class I companion, HH26IR, located 1.5' to the southwest.

Magnetic field orientation. Elongated in the north-south direction, the HH25-MMS system is separated into three distinct sources (SMM1, SMM2, and SMM3) resolved by Chen et al. (2013). The SMA observation focuses on SMM2. This is the first known detection of polarized dust emission toward this source. However, we do not detect polarization toward the very central region but in its western extension. The magnetic field at this position is tilted in the 74° direction, that is, mainly perpendicular to the projected line connecting the three sources. In this analysis, we did not compare the B-field orientation with the known outflow of the region (revealed by a VLA 3.6 cm survey) because there is strong evidence that the outflow originates from SMM1 and not from SMM2 (Bontemps et al. 1995; Chen et al. 2013).

HH211-mm

Continuum morphology at 850 μm . As observed at 230 GHz by Gueth & Guilloteau (1999), the HH211-mm submm continuum emission is compact. Also resolved with the SMA, the continuum is slightly elongated in the southwest direction, that is, perpendicular to the outflow axis.

Fragmentation. Higher resolution SMA observations also performed at 850 μm have revealed that HH211-mm hosts two sources separated by 0.3'' (Lee et al. 2009). The first, SMM1 is the protostar from which the collimated outflow originates, and SMM2, in its southwest, is responsible for the southwestern extension we observe in our analysis. Modeling the jet wiggle, Lee et al. (2010) also suggested that the HH211-SMM1 source itself might be a proto-binary source with a separation of ~5 au. Using ALMA data, Lee et al. (2019) have however recently questioned the nature of SMM2 as a secondary source. The companion source is not detected either as part of the VANDAM Perseus survey (Tobin et al. 2016).

Magnetic field orientation. The central field lines traced by the SMA observations have a north-south direction, that is, they are roughly perpendicular to the outflow direction. This average 175° orientation is consistent with the results from the TADPOL survey from Hull et al. (2014) and the SCUBA-POL results from Matthews et al. (2009). This is also consistent with the central, northeast, and northwest field lines traced at a 0.6'' resolution with the SMA by Lee et al. (2014) down to the ALMA scales presented in Lee et al. (2018). Farther away from the center, the B-field lines seem to realign in the direction of the outflow axis (see the eastern and western vectors).

HH212

Continuum morphology at 850 μm . The SMA observation reveals a disk-like shape in the direction perpendicular to the outflow, consistent with the continuum emission detected in Wiseman et al. (2001) and observed at 0.9 mm with ALMA (Codella et al. 2014).

Fragmentation. SMA observations at higher resolution than those presented in this paper have suggested that one, if not several, faint sources are located around the main body of the HH212-mms source (Lee et al. 2008; Chen et al. 2013). However, more recent ALMA observations by Codella et al. (2014) taken at a similar resolution (0.5 resolution) did neither resolve nor detect these sources. These fainter sources detected with the SMA are probably detections within HH212 flattened envelope. The VANDAM team, using VLA observations, derived a Toomre Q parameter for this source that is consistent with a marginally unstable disk, but did not detect multiplicity in the source (Tobin et al. 2020). We therefore consider the source as a single source until further analysis confirms or refutes the presence of additional dust peaks.

Magnetic field orientation. The field lines in the central plane are oriented in a northeast-southwest direction, close to the outflow axis of the source. The southern vectors seem to be following the outflow cavity walls. We note that B traced with ALMA, in contrast, is perpendicular to the outflow direction (Lee et al. 2018). The authors suggested that this orientation might be due to dust polarization arising from self-scattering at these small scales.

L483

Continuum morphology at 850 μm . Our SMA observations reveal a dust continuum elongated in the direction perpendicular to the outflow direction. The southwestern extension is consistent with the extension observed by Park et al. (2000) at 3.4 mm.

Fragmentation. L483 appears to be an isolated dense core down to the $2'' \times 1.5''$ scales traced by the SMA observations, as has been suggested by Jørgensen (2004) and Chen et al. (2013). Recent 1.2mm ALMA observation resolves the southwestern extension, with a separate continuum source detected at a 3σ level (Oya et al. 2017). Its nature was not discussed, however.

Magnetic field orientation. Polarized emission is not detected toward the center of the source, but is detected in the southwestern extension (two consistent detections). Its direction is perpendicular to the southeast-northwest outflow direction of the source and also perpendicular to the mean B-field orientation at core scales (93°) traced at $350 \mu\text{m}$ using SHARP by Chapman et al. (2013). We also have a detection in the eastern part of the source, although it is associated with weaker continuum emission (hence its high associated polarization fraction), with a B position angle of 90° . We did not take this vector into account in our calculation of the magnetic field orientation because of its discrepancy with the other two detections. If the three vectors were into account, the weighted mean B position angle would be 50° , leading to a misalignment of 55° between the magnetic field and the outflow orientation. This would place L483 in the center of the correlation observed in Fig. 3 and reinforce the general correlation we observe.

Serpens South MM18

Continuum morphology at 850 μm . The SMA continuum emission is extended in the western and southern part of the source. This extension is consistent with that found from the PdBI by Maury et al. (2019).

Fragmentation. Maury et al. (2011) found that SerpS-MM18 is separated into two sources: MM18a is the primary protostar, followed by a weaker secondary source MM18b $10''$ in its southwest. This result has been confirmed by the observations of the Serpens South complex by Plunkett et al. (2018).

Magnetic field orientation. H- and Ks-band polarization measurements have shown that the large-scale magnetic field is globally well ordered perpendicular to the main Serpens South filament, thus in an east-west direction (Sugitani et al. 2011). When we zoom in on SSMM18, the magnetic field lines are also oriented in this EW direction, with lines perpendicular to the outflow axis. The divergence of the eastern vectors could be a signature of an hourglass morphology.

Appendix B: Effect of the pixel size on the mean B-field orientation

Table B.1. Effect of the pixel size on the mean B-field orientation

| Name | B_{mean} P.A. | | | | |
|------------|-----------------|-------|-------|-------|-------|
| | 0.6'' | 0.7'' | 0.8'' | 0.9'' | 1.0'' |
| Per B1-bS | 26° | 21° | 26° | 21° | 22° |
| Per B1c | 99° | 95° | 99° | 97° | 92° |
| BHR7-MMS | 87° | 90° | 93° | 91° | 92° |
| HH25-MMS | 74° | 83° | 85° | 86° | - |
| HH211-mm | 174° | 167° | 175° | 162° | 170° |
| HH212 | 51° | 59° | 56° | 57° | 47° |
| L483 | 8° | 4° | 23° | 17° | 16° |
| Serp SMM18 | 84° | 83° | 84° | 85° | 83° |

Appendix C: Complementary tests on the mean B-field orientation estimates

Other methods were developed to calculate mean polarization angles, in particular, to analyze single-dish observations of dust polarized emission. We provide here the B-field position angle obtained from three other averaging methods. Table C.1 gathers the various estimates derived.

Column (1) provides the (arithmetic, not weighted) mean B-field orientation within the central 1000 au region. Column (2) provides the B-field orientation estimated using the technique described in Li et al. (2006). First, we computed $Q' = Q/P_i$ and $U' = U/P_i$ for each pixel in which the polarization is detected in the central 1000 au region, then averaged all values of Q' and U' . We then derived the position angle average using Q' , U' and Eq. 4. Finally, Column (3) provides the B-field position angle obtained when all the Q and U fluxes of each pixel in which the polarization is detected in the central 1000 au region are summed separately, and the position angle average was then derived from the two sums. These methods, although adapted to compute a mean B orientation in single-dish observations with many independent detections with high S/N over a wide range of physical

local conditions, may not be well adapted to interferometric data that contain only a few detections with large variations in their associated errors and that emanate from rather homogeneous local conditions and large variations in their associated errors.

The reference values we used in this analysis are reported in Table 4. The values of the B position angles estimated with the different averaging methods are extremely consistent with each other (with a standard deviation of 5° between the test and the nominal values), which is expected because the area over which the calculation was performed is small. These tests show that the main component of B in the protostellar envelopes we discussed here are, considering the intrinsic limitation of the data in hands, robust envelope-scale values, and our handling of the polarization data is therefore meaningful.

Table C.1. Results from alternative methods for the B-field position angles

| Name | B_{mean} P.A. | | |
|-----------------|-----------------|-------------------------|---------------------------------|
| | Mean (1) | Li et al. (2006) (2) | From $\Sigma U/\Sigma Q$ (3) |
| Per B1-bS | 26.1° | 23.6° | 25.9° |
| Per B1c | 99.6° | 92.0° | 90.3° |
| B335 | 54.7° | 55.0° | 54.7° |
| BHR7-MMS | 84.0° | 84.8° | 86.4° |
| CB230 | 84.7° | 85.7° | 84.6° |
| HH25-MMS | 77.4° | 78.8° | 75.6° |
| HH211-mm | 173.3° | 173.9° | 173.4° |
| HH212 | 51.1° | 59.8° | 56.6° |
| HH797 | 110.4° | 110.5° | 110.4° |
| IRAS03282 | 42.2° | 44.7° | 42.4° |
| IRAS16293-A | 139.3° | 174.0° | 173.3° |
| L1157 | 149.4° | 148.2° | 149.0° |
| L1448C | 95.0° | 94.9° | 95.0° |
| L1448N-B | 22.8° | 23.1° | 22.8° |
| L483-mm | 7.9° | 7.3° | 7.9° |
| NGC 1333 IRAS4A | 53.4° | 57.3° | 54.0° |
| NGC 1333 IRAS4B | 46.9° | 48.9° | 49.4° |
| SSMM18 | 84.7° | 79.9° | 84.0° |
| SVS13-B | 20.0° | 20.8° | 19.1° |

Appendix D: Polarization intensity and fraction maps

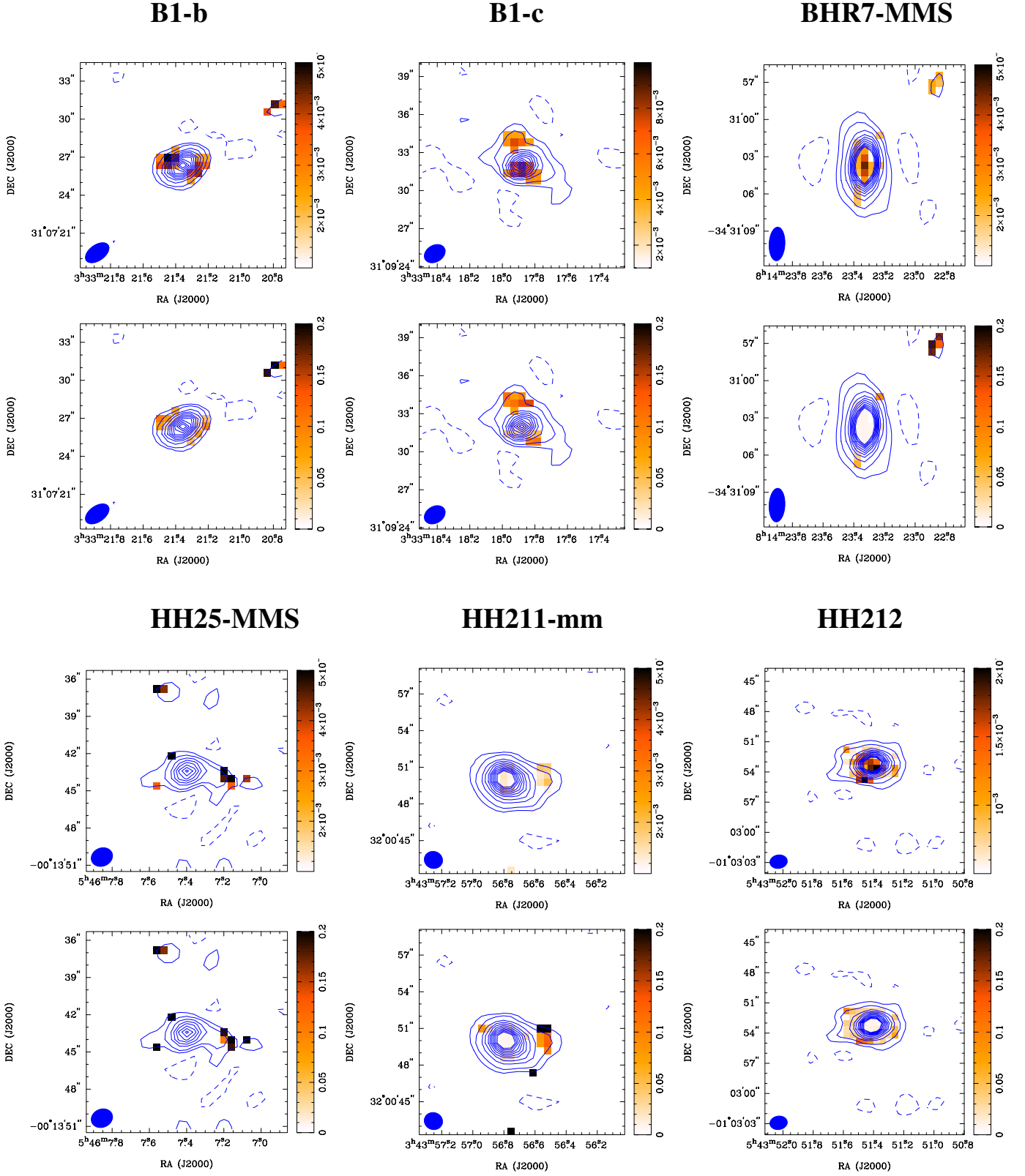


Fig. D.1. For each source, the *first row* shows the polarization intensity maps of the sample derived from the Stokes Q and U maps obtained with the SMA at $850 \mu\text{m}$. The color scale is in Jy/beam . The Stokes I contours at $-3, 5, 10, 20, 30, 40, 50, 60, 70, 80, 90,$ and 100σ are overlaid in blue. The filled ellipses in the lower left corner indicate the synthesized beam of the SMA maps. Their sizes are reported in Table 3. *Second row*: Polarization fraction map.

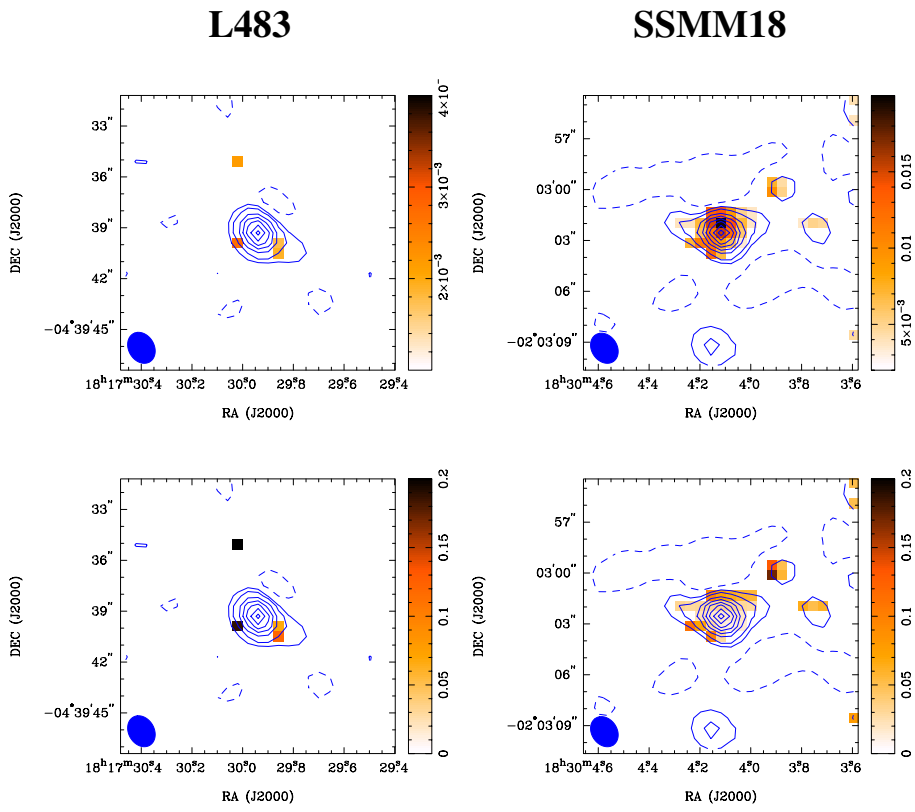


Fig. D.1. continued.

Appendix E: Velocity maps

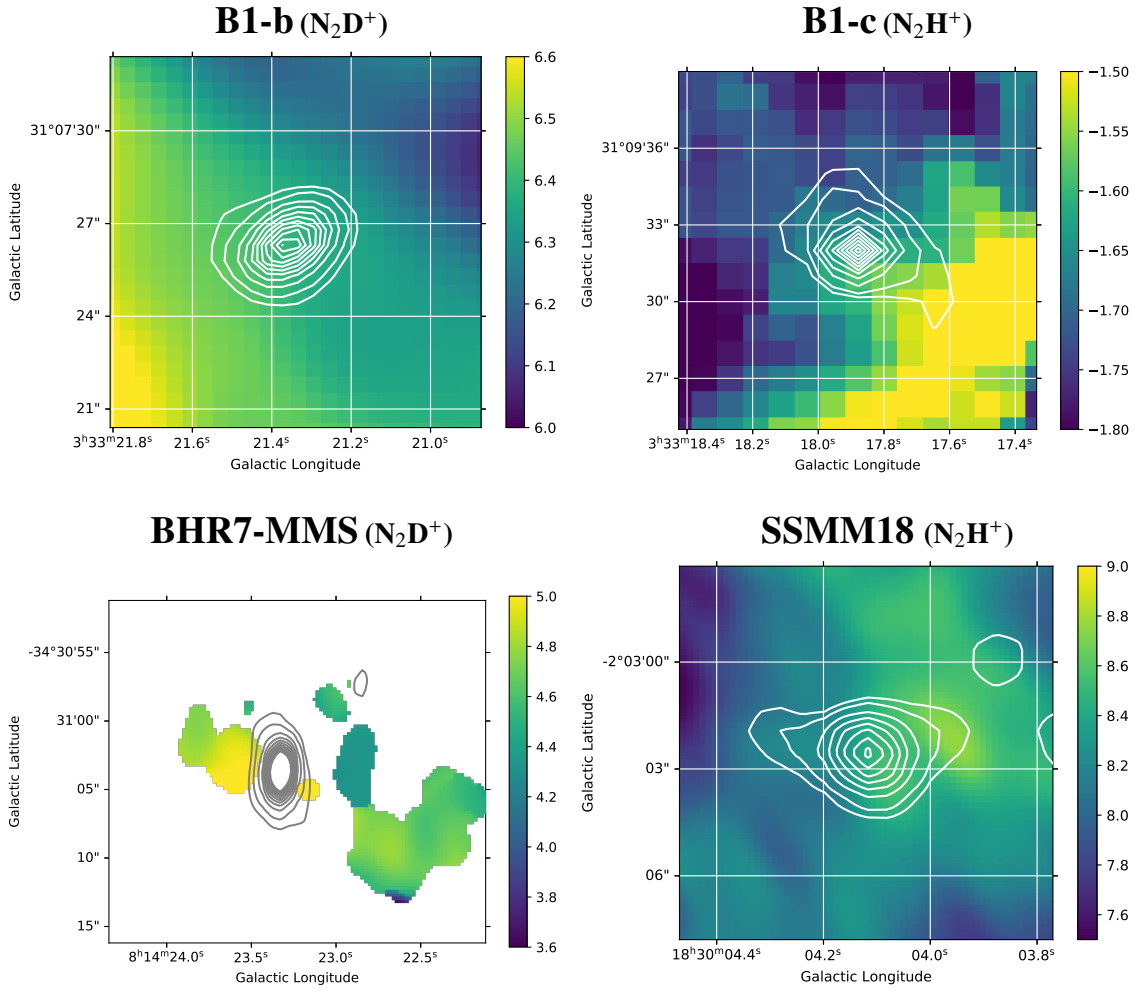


Fig. E.1. Velocity maps derived from N_2H^+ for B1-c and SSMM18, N_2D^+ for B1-b and BHR7. Data are presented in Huang & Hirano (2013), Matthews et al. (2008), and Tobin et al. (2018) for B1-b, B1-c, and BHR7, respectively. The Serpens South MM18 data come from the PdBI CALYPSO survey.